The 2011-2019 Long Valley Caldera inflation: new insights from separation of superimposed geodetic signals and 3D modeling

F. Silverii[a,b,*], F. Pulvirenti[c], E. K. Montgomery-Brown[d], A. A. Borsa[b], W. R. Neely[b]

[a] *German Research Centre for Geosciences (GFZ), Potsdam, Germany*
[b] *Scripps institution of Oceanography, University of California San Diego, La Jolla, CA, USA*
[c] *Nanjing University of Information Science and Technology, Ningliu Road, Nanjing-China*
[d] *U.S. Geological Survey, Cascades Volcano Observatory, Vancouver, WA, USA*

Abstract

Increasingly accurate, and spatio-temporally dense, measurements of Earth surface movements enable us to identify multiple deformation patterns and highlight the need to properly characterize the related source processes. This is particularly important in tectonically active areas, where deformation measurement is crucial for monitoring ongoing processes and assessing future hazard. Long Valley Caldera, California, USA, is a volcanic area where frequent episodes of unrest involve inflation and increased seismicity. Ground- and satellite-based instruments show that volcanic inflation renewed in 2011, and is continuing as of early 2021. Additionally, Long Valley Caldera is affected by the large, but spatially and temporally variable, amounts of precipitation falling on the adjacent Sierra Nevada Range.

The density and long duration of deformation measurements at Long Valley Caldera provide an excellent collection of data to decompose time-series and separate multiple superimposed deformation sources. We analyze GNSS time-series and apply variational Bayesian ICA decomposition method to isolate inflation-related signals from other processes. We show that hydrological forcing causes

*Corresponding author
Email address: silverii@gfz-potsdam.de (F. Silverii)

significant horizontal and vertical deformation at different temporal (seasonal and multiyear) and spatial (few to hundreds of km) scales that cannot be ignored while analyzing and modeling the tectonic signal. Focusing on the last inflation episode, we then improve on prior simplistic models of the inflation reservoir by including heterogeneous subsurface material properties and topography. Our results suggest the persistence and stability of the reservoir (prolate ellipsoid at about 8 km beneath the resurgent dome) and indicate a 40-50% reduction of the inflation rate after about 3 years from the inflation onset. The onset of the reduced inflation rate corresponded in time with the occurrence of a strong seismic swarm in the Caldera, but also to the temporal variation of climatic conditions in the area.
Keywords: Long Valley Caldera, GNSS data, signal decomposition, volcanic inflation, 3D heterogeneous model

---

1. Introduction

Discerning between different deformation sources, especially in tectonically active areas, is key to understanding ongoing processes and assessing future hazards. Space-geodetic techniques, such as the Global Navigation Satellite System (GNSS), have improved in the last decades, enabling detection of non-tectonic deformation (e.g., due to redistribution of water masses) occurring at different temporal and spatial scales and in various geographic and geophysical contexts (e.g., Argus et al., 2017; Drouin et al., 2016). Consequently, non-tectonic deformation may influence the interpretation of tectonic deformation and there may be interactions between the processes (e.g., Amoruso et al., 2017; D'Agostino et al., 2018; Hu & Bürgmann, 2020).

Located in the transition between the Eastern California Shear Zone (ECSZ) and the Walker Lane Belt (WLB) at the eastern edge of the Sierra Nevada range (SNR), Long Valley Caldera (LVC) is a highly tectonically-active area. It endures long-term shear and extension, frequent episodes of unrest (volcanic

inflation) and earthquake swarms (e.g., Hill et al., 2020). Large, and spatio-temporally variable, amounts of precipitation fall in the adjacent SNR (annual average ≈100 cm/yr), driving strong hydrological forcing at different spatio-temporal scales (e.g., Argus et al., 2017; Kreemer & Zaliapin, 2018). GNSS data, used extensively to study deformation at LVC, are therefore influenced by the superimposed effects of these tectonic and non-tectonic processes.

The onset of recent activity at LVC was heralded in 1980 by four M6 earthquakes (Julian & Sipkin, 1985). Since then, various instruments were deployed (e.g., seismic, gravity, geodetic) and collected measurements during multiple unrest episodes. Modeling studies have consistently identified the main source of deformation as a volumetric source located in the middle crust (6—12 km) beneath the Resurgent Dome (Hill et al., 2020, and references therein). Despite good fits overall, deformation models of different unrest episodes often resulted in localized and relatively high misfits near the LVC South Moat and along the eastern SNR front. These misfits suggest additional factors, such as the presence of secondary deformation sources (e.g., fault slip associated with earthquake swarms, fluid motion, or additional inflationary sources), effects of frictional decoupling along the South Moat Fault, or changes in lateral crustal strength, particularly between LVC and SNR (Feng & Newman, 2009; Ji et al., 2013; Langbein et al., 1995; Langbein, 2003; Lin et al., 2010; Liu et al., 2011; Marshall et al., 1997; Newman et al., 2006; Tiampo et al., 2000).

The hydrological influence on LVC is mainly related to the high precipitation falling on the adjacent SNR and the subsequent snowmelt along the western-southwestern LVC rim, which recharges a diffuse hydrothermal system (e.g., Peacock et al., 2016). These impacts were identified from runoff-related shallow seismic swarms on the south caldera margin (Montgomery-Brown et al., 2019), and by significant surface deformation, at both annual and multiyear time scales. This is related to large- and regional-scale elastic response to hydrological loading/unloading and local-scale poroelastic effects at SNR eastern edge and LVC southwestern Moat (Hammond et al., 2019; Silverii et al., 2020).

In 2011, a new episode of inflation began (Ji et al., 2013; Montgomery-Brown

et al., 2015), and has continued through two seismic swarms beneath Mammoth Mountain during February 2014 (Shelly et al., 2015) and southeastern LVC between May–November 2014 (Shelly et al., 2016), the latter representing the most prolific seismicity observed in the caldera since 1997–1998. During this time, LVC and surroundings were also affected by highly variable climatic conditions with high precipitation years in 2010–2011 and 2017–2018 and a severe drought between 2012 and 2016 (e.g., Argus et al., 2017; Kreemer & Zaliapin, 2018; Silverii et al., 2020).

Here, we analyzed horizontal and vertical GNSS time-series and applied the variational Bayesian Independent Component Analysis (vbICA) decomposition method (Gualandi et al., 2016) to isolate inflation-related signals from the effects of hydrological forcing (Sections 2, 3). We then implemented a three-dimensional numerical model to study the evolution of the recent inflation episode and assess the effect of topography and heterogeneous material properties on surface deformation (Sections 4, 5). Finally, we discussed the results and highlighted strengths and limitations of our approach (Section 6).

2. GNSS data

The continuous GNSS stations we used are operated by the National Science Foundation's Network of the Americas (NOTA) and the U.S. Geological Survey (USGS). We used publicly available daily positions processed by USGS in the North America fixed reference frame, not regionally filtered (`https://earthquake.usgs.gov/monitoring/gps/stations`, Murray & Svarc (2017)). To better constrain the spatial and temporal consistency of the different signals contributing to GNSS data, we considered an area larger than LVC and a time interval longer than the recent inflation. In particular, we selected 69 stations from Central to Southern SNR (latitude 36° N to 38.5° N, longitude -120° W to -117° W, elevation 80 m to 3900 m a.s.l., Figure 1 and Table S1) and we considered the time interval between January 1st, 2002 and October 1st, 2018. We

excluded 7 stations (CASA, KRAK, JNPR, LCOV, P628, P723, VINE) which lack data or contain substantial data gaps.

We corrected the time-series for outliers and step discontinuities at epochs corresponding to equipment changes reported in USGS site log-files and for other documented (from Nevada Geodetic Laboratory, `http://geodesy.unr.edu/NGLStationPages/steps.txt`) and undocumented offsets.

The GNSS time-series are generally characterized by long-term trends related to distributed deformation associated with the plate boundary. Deviations from the long-term trend may be attributed to large transients of tectonic – e.g., related to inflation activity (Liu et al., 2011; Montgomery-Brown et al., 2015) – and non-tectonic origin – e.g., related to variable hydrological forcing (Argus et al., 2017; Silverii et al., 2020).

To separate the different deformation sources and, in particular, to isolate the caldera inflation-related deformation, we applied the vbICA decomposition technique by Choudrey & Roberts (2003), as modified for GNSS time-series by Gualandi et al. (2016) and previously applied to separate/extract transient signals of different origin from GNSS time-series (e.g., Gualandi et al., 2017; Serpelloni et al., 2018). vbICA uses a generative model to recreate the observations, extracting the spatiotemporal information of independent deformation sources directly from the data, without imposing any explicit spatial distribution or temporal function. Since each Independent Component (IC) is described by a mix of Gaussians, that can reproduce multi-modal probability density functions commonly observed in geophysical signals, vbICA allows greater flexibility in deformation source characterization compared to classic ICA techniques. Furthermore, vbICA handles data gaps without any interpolation or assumption about their temporal behavior (Chan et al., 2003; Gualandi et al., 2016).

The GNSS displacement time-series are decomposed into a finite number of independent components (N). Each component is characterized by a weight coefficient (S), a temporal evolution (V) and a spatial distribution (U) expressing the importance of the component for each GNSS site. The contribution

from each IC at each GNSS site is obtained by multiplying the specific spatial distribution by the associated component weight, and temporal evolution. The displacement time-series at a given site can be reconstructed by linearly summing the contributions from all ICs.

To estimate the optimal analysis parameters and the proper number of ICs, we followed the methodology described in Gualandi et al. (2016), which is based on the Automatic Relevance Determination (ARD) and the estimation of the Negative Free Energy (NFE) associated with the generative model.

2.1. Removal of long-term trend

To better separate the different deformation sources, it is recommended to reduce the dataset correlation by removing the linear long-term trend from the time-series prior to vbICA (Gualandi et al., 2016).

Most of the GNSS stations in the study area started operation between 2005 and 2006, while about 30% date back to 2000 and are mostly located in LVC area. The GNSS time-series exhibit non-linear motion during the 2002–2004 and 2011–present LVC unrest episodes (Liu et al., 2011; Montgomery-Brown et al., 2015; Hammond et al., 2019), and are affected by deformation related to the highly variable hydrological conditions that affected the Western USA after 2011. To estimate the "steady-state" long-term velocity, we therefore focused on the relatively stable time interval 2005–2011, and, unlike Gualandi et al. (2017) and Serpelloni et al. (2018) which employed different methods for the prior estimation of the long-term trend, and similarly to Pintori et al. (2021), we used vbICA.

The results of vbICA application on these shortened (2005–2011) time-series (Figure S1) show that, of the $N = 4$ components selected through ARD method, the dominant component (IC1) identifies a linear signal explainable as long-term trend. IC2 and IC3 isolate seasonal and multiyear hydrology-related deformation, as revealed by their temporal behavior (see comparison with monthly and cumulative detrended precipitation at Lee Vining, location in Figure 1, data

from NOAA `https://www.ncdc.noaa.gov/cdo-web`) and spatial distribution (higher at sites in SNR area and, for the horizontal component, in LVC south-western Moat and SNR eastern edge, as previously highlighted by Silverii et al. (2020)). IC4 shows a mostly-horizontal seasonal common mode error (CME). For each site we then estimated the long-term velocity and related uncertainty by linear robust fitting of the time-series reconstructed using only the IC1 component. For this purpose, here and in Section 3.1, we used the MATLAB function *robustfit*. Note that, since temporal correlations are not considered, the resulting uncertainties might be underestimated, particularly when applied to raw time-series. The resulting velocities (Figure S2 and Table S1) are in good agreement with previous studies (e.g., Bormann et al., 2016; Hammond et al., 2016, 2019): horizontal velocities increase smoothly from ≈4 mm/yr in the Basin and Range province to ≈13 mm/yr in the central Sierra Nevada; vertical velocities generally show a slight uplift up to ≈2 mm/yr. Interestingly, we capture the minor amount of focused subsidence in western LVC previously highlighted in the "predrought period" by Hammond et al. (2019) and the westward, slightly subsiding motion of CA99 (Figure 1) due to nearby geothermal production. The detrended time-series obtained by removing the so-calculated velocities (red dots in Figure 2) show variable behaviors spanning far-field (MUSB, P468) to near-field (from south to north: P631, HOTK, RODM, WATC, BALD, PMTN, P649) sites relative to the LVC area (Figure 1).

3. Time-series decomposition results

To extract and separate the main sources of deformation, we then applied the vbICA decomposition on the detrended time-series considering the entire examined period (2002–2018.83). The ARD and NFE criteria led to 4 ICs, whose temporal (V) and spatial ($S \cdot U$) patterns and corresponding power spectral density are represented respectively in Figures 3 and S3. Note that the V_i time-series before 2005 are generally noisier because of lower available GNSS

stations.

As shown by its spatial pattern, IC1 is mostly related to inflation/deflation episodes at LVC (primarily 2003–2004 and 2011–present) plus some remaining CME in the horizontal components (c.f. Section 3.1).

Similarly to results of Section 2.1, IC4 represents a mostly-horizontal CME.

The spatio-temporal trends of IC2 and IC3 indicate mostly a hydrology-related signal at multiple temporal scales, highlighting phases of dry and wet periods. In particular, IC2 (with main power peaks at 5 and 11 years), identifies the multiyear hydrological signal, as shown by the comparison with cumulative detrended precipitation at Lee Vining. IC3 is mostly related to time-varying seasonal deformation, as shown by the comparison with monthly precipitation. Both IC2 and IC3 show a similar spatial pattern with higher vertical amplitude in the SNR area and higher horizontal amplitude at sites along SNR edges and, particularly, in LVC southwestern moat. At these sites the horizontal motion is directed perpendicular to the SNR rim with an opposite sign from the general trend. These features are compatible with the findings of Silverii et al. (2020), that highlighted an anomalously large annual horizontal signal in southwestern LVC possibly associated with water infiltration and draining within fractured rock in the Sierra Nevada range-front, and suggest that a similar non-elastic process affects the deformation also at multiyear scales.

As a further test for IC2 and IC3, we estimated the deformation expected at the GNSS sites from elastic response to the load of global terrestrial-water-storage change recorded from the joint NASA/GFZ Gravity Recovery and Climate Experiment (GRACE) and GRACE Follow-On (GRACE-FO) missions (Landerer et al., 2020). Section S1 of Supporting Material provides a detailed description of this analysis. The comparison between the time-series reconstructed from IC2+IC3 and the GRACE-modelled ones – after removal of a long-term trend – shows that the latter best reproduce the observed GNSS displacement in the vertical (amplitude and phase), but it increasingly underestimates the amplitude at sites closer to the SNR axis (Figure 4). This is consistent with

GRACE not having the spatial resolution to localize hydrological-loads along the narrow SNR, where most of the surface-load changes are expected to occur. In the horizontal, GRACE-derived displacement estimates are in phase with and represent a significant fraction of the amplitude of GNSS displacements far from the SNR. Closer to the SNR axis (especially red points in Figure 4), GRACE displacements have smaller seasonal amplitude, and do not capture the large multiyear displacement. This indicates a physical mechanism distinct from loading, since simply increasing the GRACE amplitude (by localizing SNR water storage) would not reproduce the observed GNSS signal.

3.1. Comparison between raw and IC1-reconstructed time-series

We consider now the IC1 component and the time-series reconstructed for each site using V_1, S_1 and U_1 (hereafter "IC1-reconstructed time-series"). Figure 2 shows the superposition of the raw and IC1-reconstructed time-series at selected sites.

After the beginning of the inflation in 2011.75 (epoch defined through IC1), both raw and IC1-reconstructed time-series show, in both horizontal and vertical components, a slope change occurring at the end of 2014. We therefore defined two subsequent time intervals, T1 (2011.75–2014.84) and T2 (2014.84–2018.83), where 2014.84 is the final epoch of the seismic swarm in southeastern LVC (yellow bar and top plots in Figure 2 representing the number of earthquakes occurring in LVC region – longitude: -119.1° to -118.55°; latitude: 37.5° to 37.8°; data from `https://earthquake.usgs.gov/earthquakes/`). This time, however, also roughly corresponds to a change in the multiyear hydrological trend from drought-related decreasing precipitation to renewed high precipitation, as visible in the precipitation data and in (vertical) time-series at sites far from LVC, such as MUSB (Figures 2 and 3).

We estimated velocities in T1 and T2 for both raw and IC1-reconstructed time-series (Figure S4). In the IC1-reconstructed case, we then removed the horizontal CME by estimating the median of horizontal velocities of GNSS sites at a radial distance >50 km from the resurgent dome (resulting in 1 and 0.5 mm/yr

in T1 and T2 respectively). We applied this correction in the raw case for T2, since the far-filed T2 velocities show a coherent direction and median value of 1 mm/yr; conversely, in T1 far-field velocities directions are scattered (Figure S5). The final velocity distribution is displayed in Figure 5.

The raw horizontal velocities (black arrows in Figure 5) of sites north and south of LVC show a different behavior: while the velocity magnitude diminishes at all sites from T1 to T2, those in LVC South Moat – and, with lower magnitudes, along the eastern SNR edge – experience an abrupt change of velocity direction. The raw vertical velocities in T1 generally show uplift with higher magnitude at SNR sites, gradually diminishing towards east and enhanced in LVC. Velocities in T2 show subsidence diminishing toward east, while only a few sites near the resurgent dome experience uplift.

The distribution of velocities from IC1-reconstructed time-series (red arrows in Figure 5) show deformation focused on LVC area. This is characterized by a slightly asymmetrical (elongated north-south) radial-horizontal pattern and uplift-vertical pattern centered at the resurgent dome and negligible at sites far (>50 km radial distance) from LVC, and a 54% velocity reduction from T1 to T2. This indicates that IC1 isolates the volcano-related deformation and points to a possible inflation-strength reduction in T2.

Since the vbICA decomposition determines a temporal evolution common to all sites and components, the difference between sites in LVC North and South Moats (e.g., compare the north component of P631 and BALD in Figure 2) and the strong effect of the hydrological forcing on the vertical component could influence the decomposition results. As a test, we conducted another vbICA decomposition using only the horizontal components and excluding the sites in the LVC South Moat (i.e., located south of RDOM). This test is described in detail in Section S2 of Supporting Material. The results (Figure S6) indicate a slightly lower velocity reduction (40%) between T1 and T2. The differences between the velocity in T1 and T2 at each site in the two decomposition analyses (Figure S7) reach the highest values (≈0.6 mm/yr in T1 and ≈0.9 mm/yr in T2)

at the sites north of the resurgent dome (BALD, DDMN, KRAC, P638, Figure 1), but fall within the velocity uncertainties. In conclusion, we cannot exclude some residual trade-off between inflation-related and non-tectonic processes in IC1 and IC2 components in the "all-sites and all-components" analysis and we therefore assume the previously estimated velocity change as an upper-bound value.

4. Modeling Methods

To investigate the source of the observed deformation, we tested internally pressurized ellipsoidal reservoir models embedded in an elastic medium in absence of remote tectonic stresses, assuming a negligible viscoelastic response.

4.1. Model setup

We implemented a 3D finite element method (FEM) model which includes topography and material heterogeneities using the software COMSOL Multiphysics (http://www.comsol.com/). The model domain is referred to a Cartesian reference frame centered at $[37.5°, -119°]$ and zero vertical coordinate (z = 0 m) at sea level. It consists of a crust portion of 135 x 125 x 40 km around LVC (40 km being the Moho depth in the area (Frassetto et al., 2011; Ruppert et al., 1998)) selected to embody the volume of shear-wave velocity (V_s) values from Flinders et al. (2018). The topography was implemented using the Shuttle Radar Topography Mission (SRTM) data (Farr et al., 2007) at 600 m resolution. The model geometry is represented in Figure 6a.

To avoid edge effects caused by interaction of reservoir-induced stresses with the model boundaries and to simulate far-field boundary conditions, we implemented a set of *infinite elements* at the lateral and bottom model boundaries. We imposed a fixed lower boundary, while the lateral boundaries are free to move in the vertical direction. The upper boundary is free of displacement constraints to simulate the stress-free surface.

The mesh was set in order to provide the most effective balance between element size (spatial precision) and computational memory usage (solution speed)

(Figure 6b).

To assess the accuracy of the finite element calculations, the absence of edge effects and to ensure that the geometry and mesh adopted yield sufficient sensitivity, we tested the numerical solution obtained using a homogeneous model without topography against the analytical solutions from Beauducel (2020) and Nikkhoo et al. (2017).

The study area is characterized by a considerable lateral variation of crust material properties, transitioning from the relatively low seismic wave velocities of the volcanic rocks forming the caldera fill to the higher velocities in the crystalline basement of the Sierra Block (Bernardino et al., 2019; Dawson et al., 1990; Frassetto et al., 2011; McMechan et al., 1985; Peacock et al., 2015). To reproduce this feature, we implemented the V_s values distribution from Flinders et al. (2018) (Figure 6c). From these data, we calculated the P-wave velocity (V_p) values using a two-domain distribution (delimited by the SNR border) of the V_p/V_s ratio value: 1.75 in the Sierra Block (Montgomery-Brown et al., 2019) and 1.79 elsewhere, representing a $d(Vp/Vs)$ of 3% (Bernardino et al., 2019; Frassetto et al., 2011) (Figure 6d). To estimate the density value distribution (ρ), we used the empirical relation from Gardner et al. (1974) which express ρ in terms of V_p for an average of rock types (Figure 6e). From the so-obtained values of ρ, V_p and V_s, other elastic parameters can be calculated (Figure 6f). The resulting values for all parameters agree with the ones typically used in literature for this area (e.g., Ji et al., 2013; Liu et al., 2011; Newman et al., 2006). We note that the "dynamic" parameters derived from seismic velocities are generally higher than the "static" ones estimated in laboratory experiments (e.g., Cheng & Johnston, 1981), with increasingly better agreement expected with depth (few kilometers). Therefore, we consider the elastic material properties in our model as upper bounds.

For comparison, we also implemented simpler models without topography and/or with homogeneous material properties with average values for the LVC

area (Poisson's ratio ν=0.26 and shear modulus G=18 GPa). In the model without topography, the free surface is set at the average elevation of 2300 m a.s.l..

We performed several simulations of ellipsoid inflation in different model configurations: with/without topography, homogeneous/heterogeneous material properties (detailed description in Section S3 of Supporting Material). The results show that heterogeneous material properties produce a southwest-northeast asymmetrical deformation at the surface within a radial distance from the source horizontal location of about twice the source depth (Figure S8). This variation, which is particularly evident in the horizontal components, leads to differences up to 20% in the LVC Southwest Moat compared to homogeneous material model. The velocities computed at the GNSS site locations show that heterogeneous material properties cause a variation up to 20% and 10% respectively in horizontal and vertical components at sites in LVC Southwest Moat (Figure S9).

4.2. Source inversion method

We used the estimated velocities in T1 and T2 from the IC1-reconstructed time-series at the 48 GNSS sites included in the model area (Figure 7) to infer the inflation source of the recent inflation episode.

To reduce the number of estimated source parameters, we fixed those that were well constrained by previous studies, assuming a vertical ellipsoid (dip = 90°) with 0° strike and located at the horizontal coordinates E_x = 8000 m and E_y = 20400 m (from Montgomery-Brown et al. (2015)).

The inversion was performed in COMSOL Multiphysics using the Optimization Module. We first set 5 control variables (in the form of parameters) including: ellipsoid vertical position E_z (from z=0 m, i.e. sea level, to the ellipsoid center), ellipsoid semi-axes (E_a – oriented along x-axis –, E_b – along y-axis –, E_c – vertical –, Figure 6c), and pressure change rate ΔP. We used the Nelder-Mead method (Nelder & Mead, 1965), a derivative-free solver relying on a simplex of

n+1 points, n being the number of control variables. This solver needs a prior definition of parameters starting values and ranges. We set ranges based on parameter distributions from previous studies and starting values in agreement with the best-fit solution for the 2011-2015 inflation by Montgomery-Brown et al. (2015) (Table 1 shows parameters ranges and initial values). The solver is set to perform a maximum number of 100 model evaluations. During each evaluation it tests different control variable values, which are properly scaled to fall within their defined ranges, and adjusts them accordingly to minimize the objective function (L_2-norm of the difference between observed and modeled deformation). The number of model evaluations is chosen so that the convergence rate shows no significant improvement of the objective function value with further model evaluations. The convergence rate is controlled by an optimal tolerance parameter, which after trial and error tests was set at 0.01.

For the T1 interval, we inverted the velocities considering different model configurations, with/without topography and homogeneous/heterogeneous material properties (as described in Section 4.1). As a comparison, we also inverted the velocities estimated from the raw time-series. However, the vertical velocities in this case show strong (hydrological) deformation at large spatial scales (Section 3.1) that would inevitably bias the solution. For this comparison, we therefore first removed this long-wavelength deformation by fitting a ramp to the distribution of vertical velocity values along longitude over the all studied area, but excluding those of GNSS sites at a radial distance <50 km from the resurgent dome. The resulting velocities distribution are shown in Figure 8 (black arrows).

For the T2 interval, we considered only the topography-heterogeneous case. We also performed an additional test inverting only for ΔP and fixing all other parameters values as the best model from the corresponding T1 case.

As a further comparison, and to check the dependence of the COMSOL inversion against starting values, we ran an additional inversion based on analytical solution (flat-homogeneous) using the Markov Chain Monte Carlo (MCMC) method employing the algorithm from Anderson & Segall (2013). In this case, the ellip-

soid minor semi-axes are intrinsically equal ($E_a = E_b$), but we also inverted for dip, strike and horizontal position.

5. Inflation source inversion results

Inversion results for all cases are summarized in Table 1. The volume variation rate was estimated by numerically integrating the displacements over the ellipsoid surface. For the analytical MCMC inversion, we used the formula by Cervelli (2013). Figure 7 shows observed and modeled velocities for the IC1-reconstructed time-series case (corresponding residuals in Figure S10). Figure 8 displays the analogue map for the raw time-series case. A clearer comparison for T1 is shown in Figures S11 and S12.

The source inversion results for T1 are consistent in all the tested cases, with the best-fit model being a prolate ellipsoid with aspect ratio $E_c/mean(E_a, E_b) \approx 1.6$ and located at ≈8100 m beneath the free surface ($E_z \approx$ -5800 m). Despite the trade-off between ellipsoid dimensions and pressure change (e.g., Fialko et al., 2001), the volume change rate is well constrained at $\Delta V \approx 9{\cdot}10^6$ m^3/yr. In all cases E_a is about 1.1 times higher than E_b, probably because of the observed north-south asymmetry in the horizontal deformation pattern. E_a/E_b is generally slightly lower in the heterogeneous case since heterogeneous material properties account for part of the asymmetry by reducing the deformation amplitude in south-west LVC (Section S3 and Figures S8 and S9 in Supporting Material). In the heterogeneous case, the source is generally bigger (of 25% with IC1 time-series and of 7% with raw time-series) and deeper (of 11% with IC1 time-series and of 2% with raw time-series) than the homogeneous case, but with similar depth/source-dimension ratio (≈1.5). In particular, being the volume of material in which the source is located surrounded by stiffer material (Figure 6), the source is bigger and deeper in order to reproduce the deformation magnitude and spatial distribution, particularly in the eastern/north-eastern side of LVC (Figure 7). In the case of raw velocities inversion, the smaller differences between the inverted sources are probably due to the noisier velocity distribu-

tion, as suggested also by the resulting higher root mean square error (RMSE) values.

The results for the IC1 case provide a good fit with mostly scattered residuals (RMSE $\approx$ 1.25 mm/yr). The results obtained with velocities from raw time-series show higher residuals (RMSE $\approx$ 1.7 mm/yr), with the horizontal residuals in the LVC South Moat directed perpendicularly to the SNR rim. This residual pattern is similar to results of previous studies for the same inflation period (Ji et al., 2013; Montgomery-Brown et al., 2015) and suggests the remaining effect of hydrological deformation (Section 3.1). The opening pattern of residuals north of LVC could imply the presence of some unmodeled deformation related to an additional extensional source along the Mono/Inyo crater chain, as hypothesized for previous unrest episodes (Feng & Newman, 2009; Marshall et al., 1997). However, as we will discuss further in Section 6.1, the peculiar multiyear trend shown by sites on the SNR east edge (Section 3.1) suggests some contribution of non-tectonic deformation.

The inversion for the T2 interval suggests a slightly deeper ($Ez \approx$ -7500 m) source with similar aspect ratio and a source strength reduction of $\approx$40% from T1 ($\Delta V \approx 6.4{\cdot}10^6$ m^3/yr). A consistent value of ΔV ($\approx 5.2{\cdot}10^6$ m^3/yr) is retrieved also in the additional test for ΔP, providing a $\approx$50% reduction from the corresponding T1 case.

The analytical MCMC model solution is in good agreement with the results of the numerical model (Table 1, Figure S13), with well constrained horizontal position ($E_x \approx$ 8000 m and $E_y \approx$ 20000 m), depth of about 9000 m below the surface, aspect ratio of 1.25 and 60% ΔV reduction from T1 to T2. Dip and strike angles different from 90° and 0° (respectively 70° and 23° in T1, and 83° and 47° in T2) result to better reproduce the asymmetrical deformation pattern.

6. Discussion and Conclusions

6.1. Signal decomposition

In this work, we highlighted the presence of superimposed deformation processes in LVC and the complexity in disentangling them. Only a few studies have previously used decomposition techniques on deformation records at LVC, mainly to isolate the tectonic signal (mostly volcanic inflation) from noise and systematic survey errors (e.g., Langbein, 2003; Lin et al., 2010; Marshall et al., 1997; Savage, 1988). In particular, Ji et al. (2013) applied PCA on the GNSS horizontal time-series over a recent time interval (2009–2012), but excluded the sites at LVC South Moat because of anomalously large seasonal deformation. Our application of vbICA isolated the inflation signal related to the most recent unrest episode in addition to previous (after 2002) minor inflation/deflation episodes. Furthermore we confirmed the findings of Silverii et al. (2020) regarding a strong seasonal (horizontal) deformation at the GNSS sites in LVC Southwest Moat and eastern SNR edge and highlighted a similar anomalous behavior also at the multiyear scale. According to IC2, these sites are indeed characterized by higher deformation, oriented perpendicular to the SNR rim and with opposite sign compared to the general large-scale trend. In particular, they show alternating behavior moving away from SNR during high-precipitation periods, and vice-versa in drought periods. This is evident in the pattern of velocities estimated from the IC2-reconstructed time-series in T1 (drought period) and T2 (high-precipitation period) (Figure 9). Considering this effect is important for several reasons. (i) It can contribute to the horizontal deformation asymmetry between North and South Moats in LVC. In this regard, it could explain part of the north-south asymmetry in the strain rate distribution around LVC observed by Hammond et al. (2019), since their "drought period", lasting until 2016.7, possibly includes part of the trend change due to hydrological forcing. (ii) It could contribute to residual patterns that are often referred to additional sources beneath Mono-Inyo craters and in the LVC South Moat, possibly leading to inaccurate estimations of these sources features. (iii) LVC Southwest Moat

being the area of recharge, flow and discharge of the LVC hydrothermal system (Peacock et al., 2016), a possible contribution from the latter in the highlighted deformation can be speculated.

Applying vbICA to estimate the long-term trend of GNSS time-series, we also showed that this approach is efficient for estimating the linear trend in presence of non-linear transient signals. In general, this is particularly important for shorter time-series (e.g. those of stations installed after 2007-2008 in LVC), for which the trend estimation could be biased by the presence of multiyear transient signals.

In general, using decomposition techniques such as vbICA has the advantage of separating the main deformation sources and therefore allows inferences about their main features. This is very useful in regions such as LVC where different processes overlap. The main disadvantages, however, are that (i) looking for common features at multiple stations, these techniques inevitably cause the loss of some local and more detailed features, e.g. the possible effect of secondary inflation sources for LVC; (ii) as discussed in Section 3.1, the decomposition results could be biased by signals that are stronger at some stations/components than others. The additional tests and multiple inversion models we ran, however, show that our results are robust in describing the evolution of the inflation at LVC.

Different methods have been proposed to separate multiple signal sources in GNSS time-series recorded in volcanic areas, such as PCA or Multichannel Singular Spectrum Analysis (M-SSA) (Walwer et al., 2016). We chose vbICA due to its expected better performance in separating and representing the signal sources. This mostly relies on the release of constraints/assumptions such as orthogonality between the components and the normal distribution of data projected onto the components, and on the requirement of independence, instead of uncorrelation, between the components (Gualandi et al., 2016). In future works looking at more detailed/local features of LVC system, and possibly combining different kinds of data, it would be worth testing the performance of different

decomposition techniques.

An alternative approach would be to model the non-tectonic deformation sources using independent information, such as precipitation records for elastic response to surface load. This might be done relatively easily for large scale vertical deformation, but it would be complicated for the local anomalous horizontal deformation. In general, when interpreting deformation data in LVC, and in other similar contexts, it is important to keep in mind the possible presence of different superimposed processes.

6.2. Inflation source

The effects of topography and lateral and depth-variable material properties in LVC were proposed as a possible contribution to the observed northeast-southwest asymmetry of the inflation-related deformation and to the higher residuals in the Southwest Moat and SNR edge (e.g., Feng & Newman, 2009; Lin et al., 2010; Liu et al., 2011; Montgomery-Brown et al., 2015; Newman et al., 2006). A few previous evaluations of the effect of these factors exist, mostly consisting of simplified axisymmetric, horizontally layered, models (Battaglia & Segall, 2004; Long & Grosfils, 2009; Magni et al., 2008; Pepe et al., 2010). In our study, we systematically investigated the effect of realistic topography and 3D elastic heterogeneous material properties through both forward modeling the inflation-related deformation and inverting measured velocities to infer the source properties.

Forward models show that, while topography has a negligible contribution, material heterogeneity causes a clear northeast-southwest asymmetry in the deformation pattern with up to 20% variation with respect to the homogeneous material, within a distance from the source of approximately twice the source depth. This effect could in principle be resolved by accurate and densely distributed measurements in the source area. As revealed by simulated velocities at the GNSS locations in LVC (Figure S9), the effect of heterogeneous material is particularly pronounced at sites in the LVC Southwest Moat, which is also an area where remaining residuals from inflation modeling needed the inclusion of

additional inflation/extensional sources (e.g., Langbein et al., 1995; Langbein, 2003).

Similarly to Battaglia & Segall (2004) and Long & Grosfils (2009), our inversion results show that the consideration of heterogeneous material properties mostly affects the resulting source dimension and depth. This also agrees with outcomes from studies of other volcanic areas considering 3D material heterogeneities (e.g., Masterlark et al., 2016). The difference in horizontal axes of our best-fit numerical models might account for part of the deformation asymmetry. The role of the material heterogeneities could then be more important when the horizontal axes are assumed to be equal. Indeed, the difference between the horizontal axes diminishes in the heterogeneous cases (see E_a/E_b values in Table 1). The results from the analytical model suggest that the asymmetry could be also partly accounted for by a slightly tilted and rotated ellipsoidal source. The GNSS network in LVC is in principle spatially dense enough to resolve the effects of material heterogeneities, and our inverse models show that heterogeneous models provide a slightly better fit of the observations, especially for the horizontal deformation. This improvement (up to 0.2 mm/yr in RMSE) is, however, low compared to data uncertainties, in particular for the raw time-series. The effects of material heterogeneities could be therefore hidden-by/secondary-to the complexities due to additional sources of deformation/noise affecting measurements, such as non-tectonic (hydrological) processes. More spatially-dense InSAR data could help to highlight the effect of material heterogeneities.

Our inferred inflation source, a prolate ellipsoidal reservoir at about 8 km beneath the resurgent dome, is consistent with findings from previous studies of both same inflation episode and previous ones (Hill et al., 2020, and references therein), suggesting the persistence and stability of the LVC reservoir. The volume variation rate of $\Delta V \approx 9{\cdot}10^6$ m^3/yr in the first 3.1 years (T1 interval) is consistent with the results of Montgomery-Brown et al. (2015) over a similar time period and is similar to that of the 1990–1994 inflation interval ($7{\cdot}10^6$ m^3/yr; Marshall et al. (1997)). Even if the inflation rate is much smaller, the total accumulated volume change over the present study period 2011.75–2018.83

($\approx 53{\cdot}10^6 m^3$) is within the range of values estimated for the 1997–1998 episode (e.g., Newman et al., 2006, and references therein).

Our analysis indicates a temporal variation of the inflation rate, with a 40-50% reduction after about 3 years from the inflation onset. As discussed in Sections 3.1 and S2, this reduction represents a high-end estimation and we expect that a slightly lower value (30-40%) would result using only the data less affected by the hydrological forcing. The onset of the reduced inflation rate corresponded in time with the occurrence of a strong seismic swarm in the Caldera, whose activity was initiated and sustained by a pressure transient associated with low-viscosity fluid, likely released from underlying magma (Shelly et al., 2016). Similar examples of seismic swarms possibly associated with decreased inflation rate occurred at other volcanic systems as Three Sisters, Oregon, (Riddick & Schmidt, 2011) and Yellowstone (Chang et al., 2010). The pressure change might indicate that the swarm fractured the rock, making it more permeable and providing a pathway through which fluids could leak out. On the other hand, the time of this reduction also corresponds to the temporal change of climatic condition in independent precipitation data. This superimposition of different deformation sources could lead to an inaccurate estimation of the inflation evolution. This temporal correlation could also indicate that the hydrological forcing has a role in modulating the volcanic activity, as suggested by Hammond et al. (2019). The confirmation/confutation of this hypothesis would require additional study and represents a potentially interesting topic for future work to better understand the LVC system and, more generally, the possible interplay between hydrological forcing and volcanic activity.

In our models we employed elastic materials, however, other material behaviors could be involved, including poroelastic, non-linear rheology. Poroelastic behavior will likely be important for verifying geophysical signals related to the hypothesis of second-boiling and ascent of low-viscosity aqueous fluids (e.g., Hildreth, 2017; Prudencio & Manga, 2019) and contributions to deformation from the hydrothermal system (Peacock et al., 2016). The latter, in

particular, would be very interesting considering the temporal and spatial (in the South-West Moat) correlation between hydrological forcing and deformation within the caldera. There are also other known sources of deformation including geothermal energy production, and as-yet unobserved local deformation related to seismic swarms, as well as tilt and strain data that could be used to study these more localized processes.

The density and long duration of deformation measurements of the magmatic system at LVC provide an excellent collection of data for time-series decomposition with the vbICA method and separation of multiple superimposed deformation sources while highlighting differing physical source processes. The increased model complexity enabled by the FEM methodology presented here, which includes topography and heterogeneous material properties, allows us to assess some complexities that cannot be addressed by simpler, yet computationally efficient models.

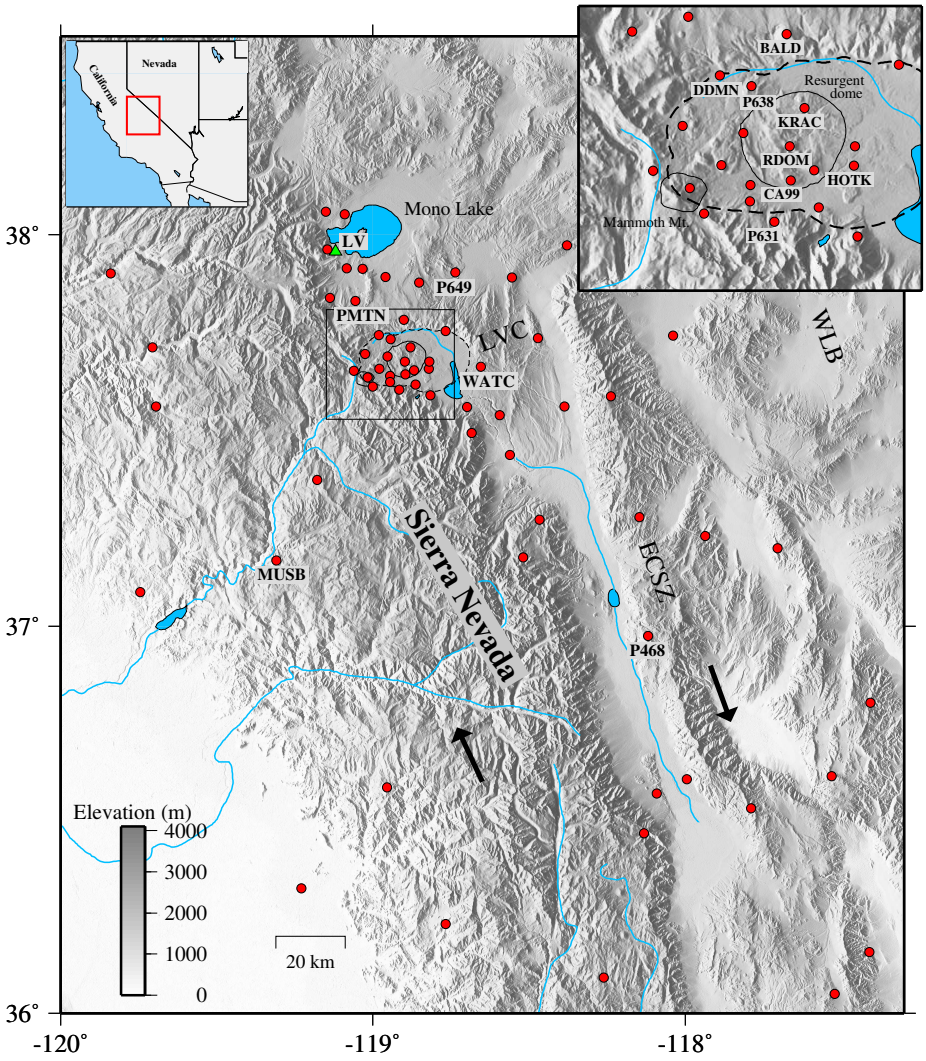

Figure 1: Geographic area and location of the GNSS stations (red circles). The green triangle indicates Lee Vining rain gauge (LV). The black arrows represent the direction of tectonic shear. Dashed and solid lines delineate Long Valley Caldera, resurgent dome and Mammoth Mountain contours. The top-right inset shows a zoomed region around LVC (black rectangle in the map).

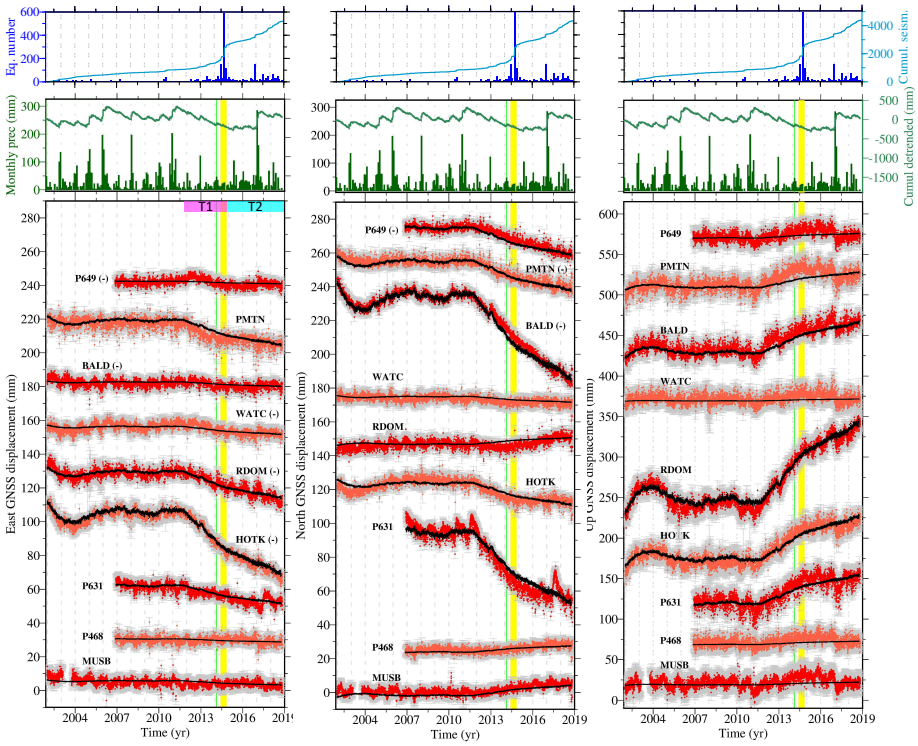

Figure 2: GNSS detrended time-series at selected sites (location in Figure 1) as raw time-series (red dots) and IC1-reconstructed time-series (black dots). The minus symbol in brackets following the station ID indicates that the time-series have been reversed along the y-axis for sake of plot clarity. The green and yellow vertical bars show the time duration of the seismic swarms respectively in Mammoth Mountain and southeastern LVC. The magenta and cyan horizontal stripes indicate the time intervals T1 and T2. As a comparison, the top plots show the cumulative detrended (green line) and monthly precipitation (dark-green vertical bars) at Lee Vining rain gauge (location in Figure 1) and the earthquakes number (weekly binned – blue bars – and cumulative – light-blue line) occurred in LVC region.

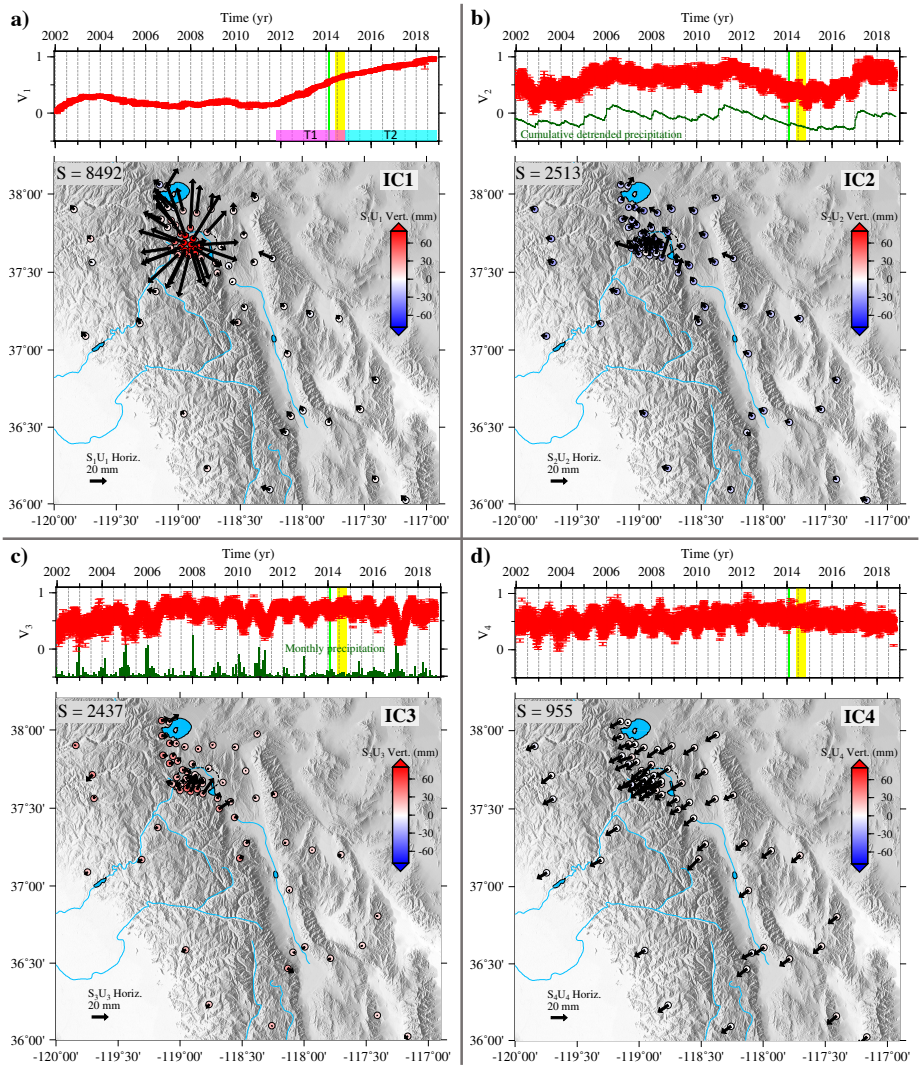

Figure 3: Results of the vbICA decomposition: each quadrant represents the temporal evolution (V, top – red dots with vertical bars representing one standard deviation errors) and map view of the spatial response ($S \cdot U$, bottom) of the 4 ICs. The weight S (mm) of each IC is indicated in the upper-left corner. Time-series: the green line (in IC2) and vertical bars (in IC3) represent respectively the cumulative detrended and monthly precipitation at Lee Vining; the green and yellow stripes show the time duration of the seismic swarms respectively in Mammoth Mountain and southeastern LVC. Maps: the black arrows and the color-coded circles respectively indicate the horizontal and vertical responses. The spatial response describes the directions along which the GNSS sites move and the arrow length and the circle color are proportional to the contribution of the specific component at every station.

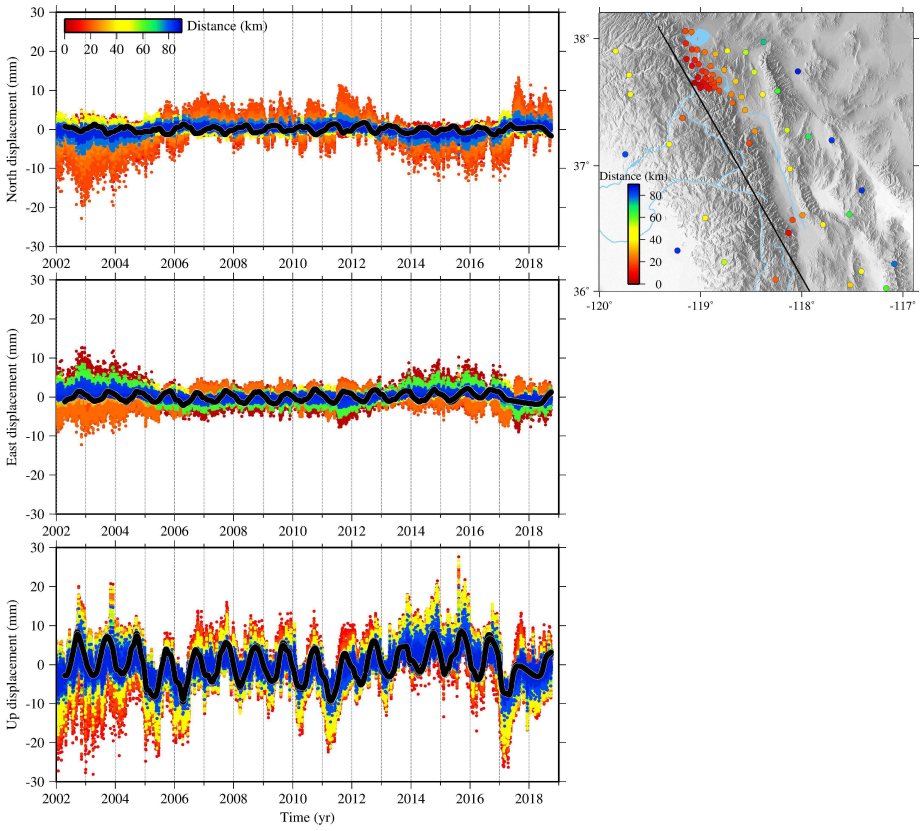

Figure 4: Comparison between (IC2+IC3)-reconstructed time-series (color-coded) and GRACE-modelled time-series (black lines). As indicated in the map inset, the (IC2+IC3)-reconstructed time-series are color-coded with colors indicating the GNSS sites distance from the SNR topographic divide (black line in the map). Note: the GRACE data after 2017 are more scattered because of missing observations.

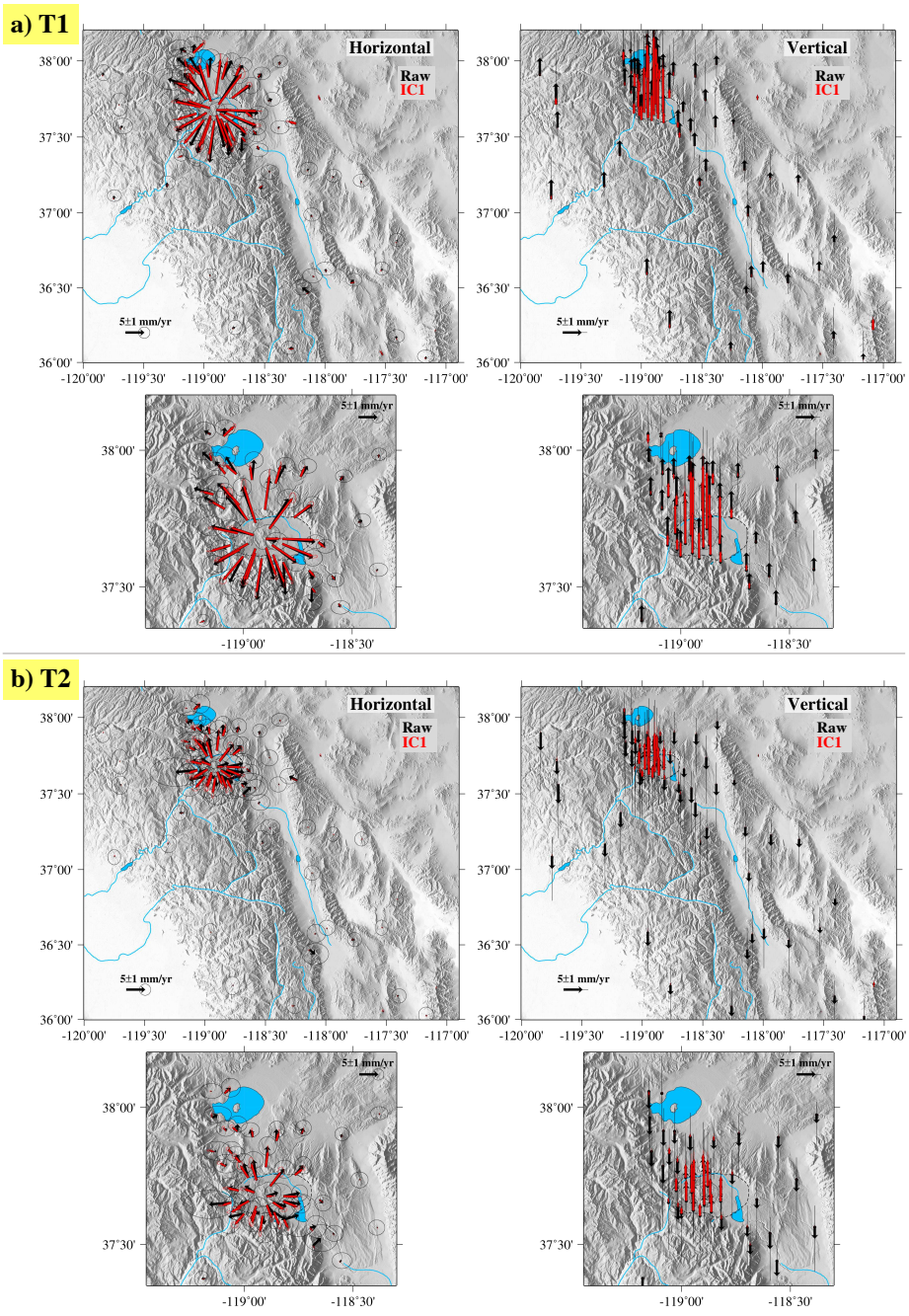

Figure 5: Maps of horizontal (left) and vertical (right) velocities estimated in the T1 (a) and T2 (b) time intervals. The black and red arrows (with 68% CI ellipses) correspond to the velocities estimated respectively from the raw and IC1-reconstructed time-series. The smaller plots show enlarged maps of LVC area.

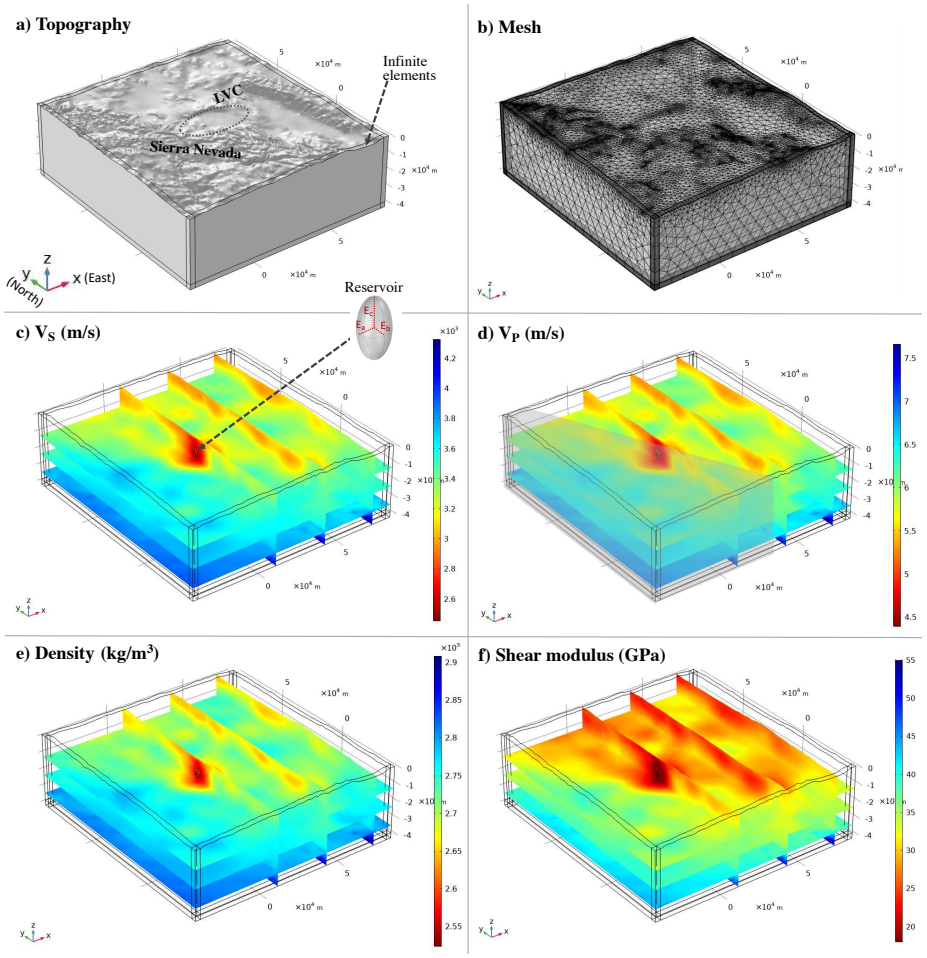

Figure 6: Three-dimensional FEM model domain setup: model domain geometry (a), mesh (b), V_s velocity spatial distribution from Flinders et al. (2018), and location and geometry of the ellipsoidal reservoir (c), V_p velocity spatial distribution derived from V_s assuming V_p/V_s values of 1.75 in the Sierra Block (shaded area) and 1.79 elsewhere (d), density (ρ) distribution derived from V_p through the empirical formula of Gardner et al. (1974) (e), shear modulus distribution derived from V_p, V_s and ρ (f).

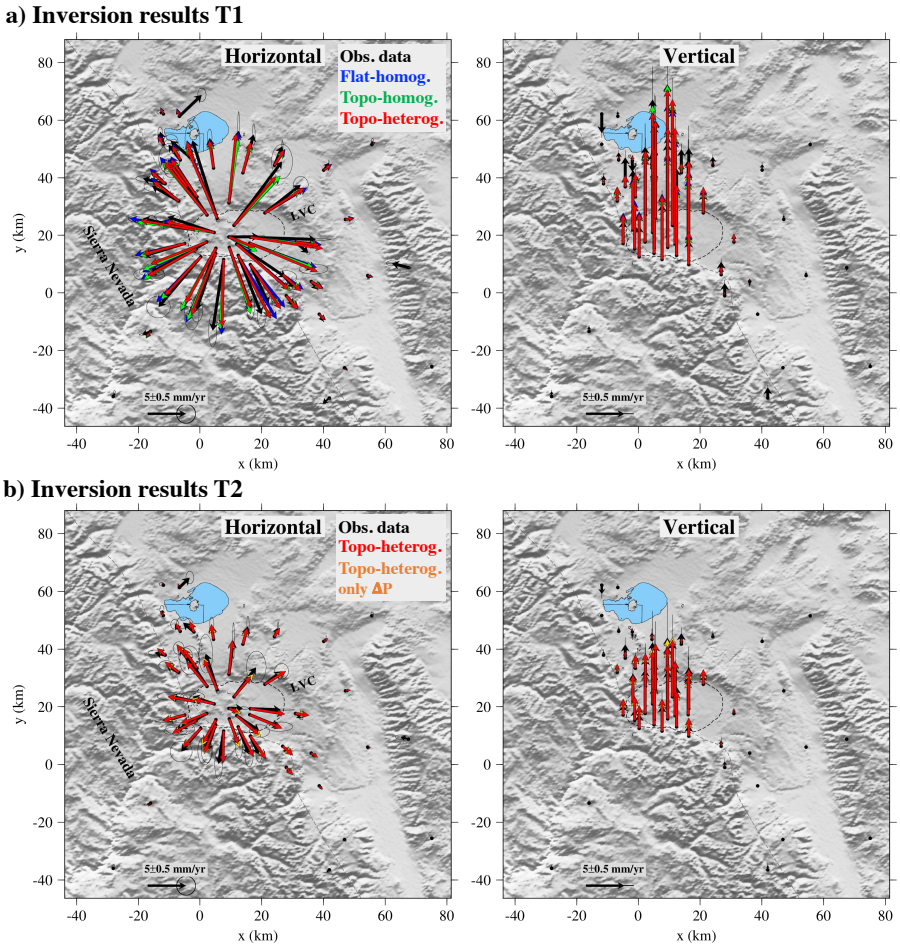

Figure 7: Comparison between observed (from IC1-reconstructed time-series, black arrows – corresponding to the red arrows in Figure 5) and modeled (colored arrows) velocities in T1 (a) and T2 (b). The corresponding residuals distribution is displayed in Figure S10 of Supporting Material. A clearer comparison for T1 is shown in Figure S11 of Supporting Material. Ellipses represent 95% CI.

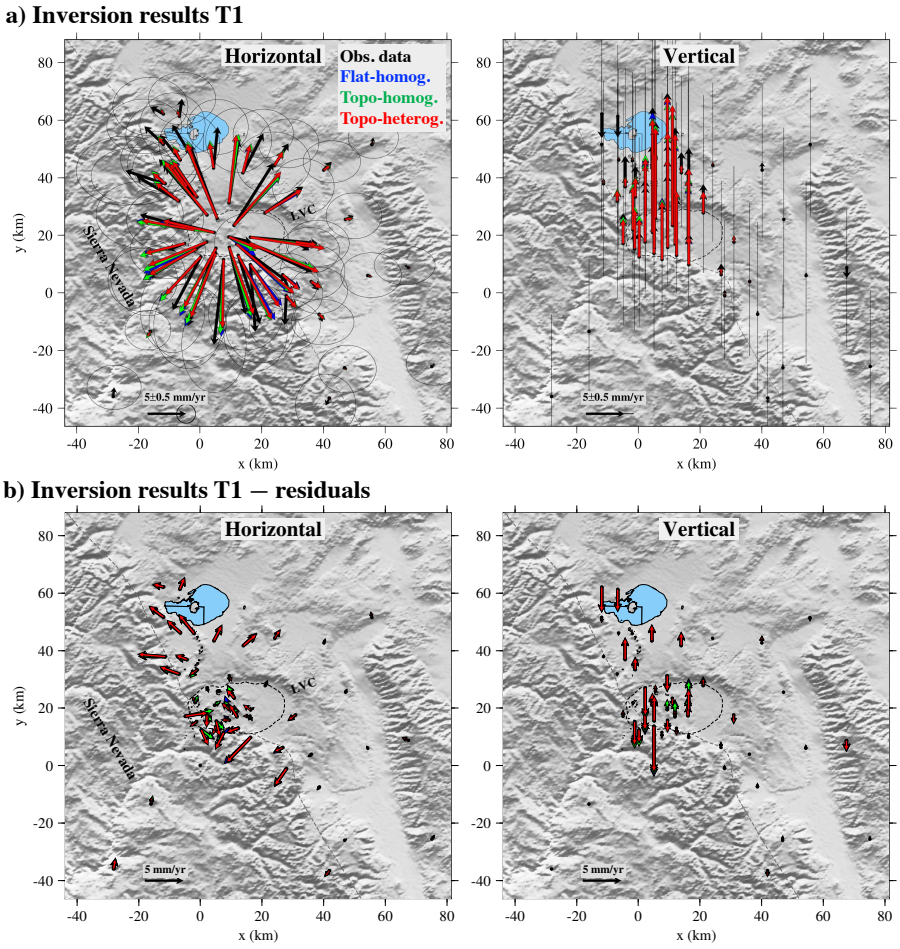

Figure 8: Comparison between observed (from raw time-series, black arrows – corresponding to the black arrows in Figure 5) and modeled velocities (colored arrows) in T1 (a) and corresponding residuals (b). A clearer comparison for T1 is shown in Figure S12 of Supporting Material. Ellipses represent 95% CI.

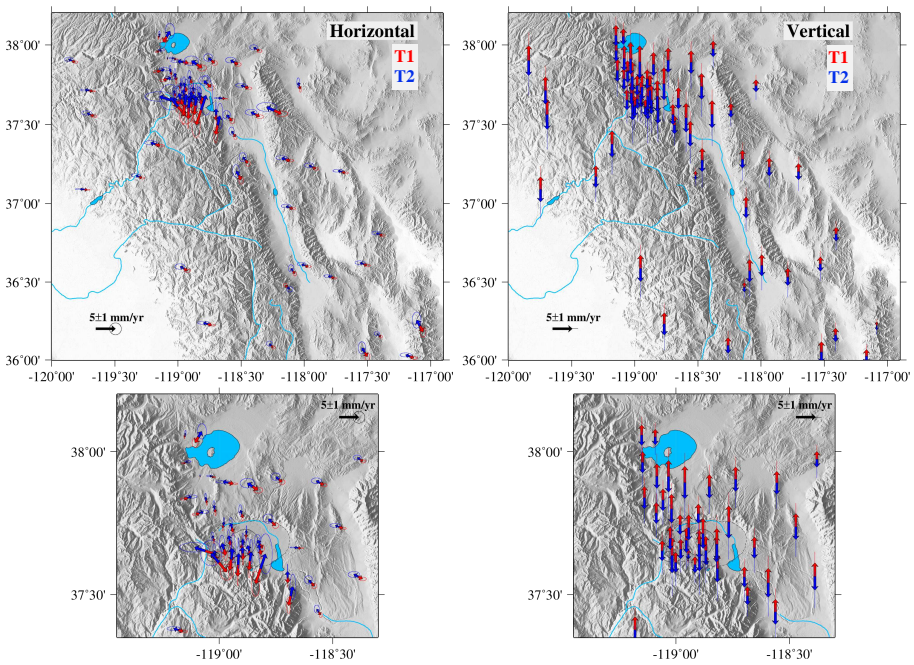

Figure 9: Maps of horizontal (left) and vertical (right) velocities estimated in the T1 (red) and T2 (blue) time intervals from the IC2-reconstructed time-series. Ellipses represent 68% CI.

Table 1: Inflation source inversion results. The values in square brackets represent the parameters inversion range, while "s.v." indicates the inversion starting value. E_z values are referred to the sea level – with positive z upward. The values in brackets in the E_z column represent the source depth below the free surface (obtained by adding the average elevation of 2300 m). Where specified, results refer to inversion of velocities estimated from the raw time-series, all other cases are for velocities from IC1-reconstructed time-series. "N" and "C" in the ΔV column refer respectively to computations through numerical integration and through the analytical formula from Cervelli (2013). "H" and "V" in the RMSE column refer respectively to horizontal and vertical components. "MCMC" refers to the Markov chain Monte Carlo inversion, where we indicated also the 95% lower and upper bounds.

Test	$\mathbf{E_a}$ **(m)** [100:4000] s.v.=1500	$\mathbf{E_b}$ **(m)** [100:4000] s.v.=1500	$\mathbf{E_c}$ **(m)** [100:4000] s.v.=1500	$\mathbf{E_z}$ **(m b.s.l.)** [-15000:0] s.v.=-6000	$\mathbf{\Delta P}$ **(MPa/yr)** [1 : 20] s.v.=10	$\mathbf{E_a/E_b}$	$\mathbf{E_c/}$ $\mathbf{mean(E_a, E_b)}$	$\mathbf{\Delta V}$ $(\mathbf{10^6 m^3/yr})$	**Residuals RMSE (mm/yr)**
T1 (raw t.s.) Flat- homog.	1880.7	1633.5	2757.8	-5466.9 (7766.9)	5	1.15	1.57	7.85 (N)	1.68 (H) 1.83 (V)
T1 (raw t.s.) Topogr. - homog.	1833.7	1615.4	2955.4	-5442.3 (7742.3)	5	1.14	1.71	8.22 (N)	1.61 (H) 1.81 (V)
T1 (raw t.s.) Topogr. - heterog.	1783.4	1676.5	3135.9	-5596.4 (7896.4)	5	1.06	1.81	9.52 (N)	1.70 (H) 1.69 (V)
T1 Flat- homog.	1432.9	1340.3	2476.1	-5784.3 (8084.3)	10	1.07	1.78	8.93 (N)	1.36 (H) 1.32 (V)
T1 Topogr. - homog.	1973.5	1782.5	2568.3	-5782.9 (8082.9)	5	1.11	1.37	8.14 (N)	1.22 (H) 1.34 (V)
T1 Topogr. - heterog.	1981.7	1868.9	3046.1	-6677.9 (8977.9)	5	1.06	1.58	11.2 (N)	1.19 (H) 1.24 (V)
T2 Topogr. - heterog.	1258.6	1244.6	2260.4	-7446.0 (9746.0)	8.8	1.01	1.80	6.45 (N)	0.63 (H) 0.61 (V)
T2 Topogr. - heterog. (only ΔP)	1981.8	1868.9	3046.1	-6677.9 (8977.9)	2.34	1.06	1.58	5.22 (N)	0.55 (H) 0.57 (V)
T1 (MCMC) Flat - homog.	3181.2 [L95: 1073.6] [U95: 3899.8]	3181.2 [L95: 1073.6] [U95: 3899.8]	3866.4 [L95: 1004.9] [U95: 3931.4]	-6817.4 (9117.4) [L95: -10960] [U95: -4489.7]	1.24 [L95: 0.81] [U95: 24.9]	1	1.22	8.58 (C)	1.26 (H) 1.26 (V)
T2 (MCMC) Flat - homog.	2527.6 [L95: 655.19] [U95: 3911.8]	2527.6 [L95: 655.19] [U95: 3911.8]	3134.9 [L95: 474.08] [U95: 3923]	-6607.9 (8907.9) [L95: -12376] [U95: -3073.7]	1.12 [L95: 0.29] [U95: 24.3]	1	1.31	3.96 (C)	0.60 (H) 0.58 (V)

Acknowledgments

We thank Paul Segall and an anonymous Reviewer for the accurate and insightful review. We are grateful to Adriano Gualandi for providing the vbICA decomposition code and for the useful advices about its application. We thank Eleonora Rivalta and her research group at GFZ, Virginie Pinel and Katy Chamberlain for the helpful discussions. We are thankful to John Langbein for his thorough comments and precious suggestions that improved the first version of this manuscript.

All raw data are available from public databases: the GNSS data are available at the USGS website `https://earthquake.usgs.gov/monitoring/gps/stations`; the Lee Vining precipitation data at the NOAA website `https://www.ncdc.noaa.gov/cdo-web`; the seismicity data were retrieved from the USGS website `https://earthquake.usgs.gov/earthquakes/`.

Figures were produced using the Generic Mapping Tools software package (Wessel et al., 2013).

Any use of trade, firm, or product names is for descriptive purposes only and does not imply endorsement by the U.S. Government.

References

Amoruso, A., Crescentini, L., & Chiaraluce, L. (2017). Surface temperature and precipitation affecting GPS signals before the 2009 L'Aquila earthquake (Central Italy). *Geophysical Journal International*, *210*, 911–918. doi:10.1093/gji/ggx210.

Anderson, K., & Segall, P. (2013). Bayesian inversion of data from effusive volcanic eruptions using physics-based models: Application to Mount St. Helens 2004–2008. *Journal of Geophysical Research: Solid Earth*, *118*, 2017–2037. doi:10.1002/jgrb.50169.

Argus, D. F., Landerer, F. W., Wiese, D. N., Martens, H. R., Fu, Y., Famiglietti, J. S., Thomas, B. F., Farr, T. G., Moore, A. W., & Watkins, M. M. (2017). Sustained water loss in California's mountain ranges during severe drought from 2012 to 2015 inferred from GPS. *Journal of Geophysical Research: Solid Earth*, *122*. doi:10.1002/2017JB014424.

Battaglia, M., & Segall, P. (2004). The Interpretation of Gravity Changes and Crustal Deformation in Active Volcanic Areas. *Pure and Applied Geophysics*, *161*, 1420–9136. doi:10.1007/s00024-004-2514-5.

Beauducel, F. (2020). Mogi: point source of dilatation in elastic half-space. *MATLAB Central File Exchange. Retrieved September 1, 2020.*, . URL: https://www.mathworks.com/matlabcentral/fileexchange/25943-mogi-point-source-of-dilatation-in-elastic-half-space.

Bernardino, M. V., Jones, C. H., Levandowski, W., Bastow, I., Owens, T. J., & Gilbert, H. (2019). A multicomponent Isabella anomaly: Resolving the physical state of the Sierra Nevada upper mantle from Vp/Vs anisotropy tomography. *Geosphere*, *15*, 2018–2042. doi:10.1130/GES02093.1.

Bormann, J. M., Hammond, W. C., Kreemer, C., & Blewitt, G. (2016). Accommodation of missing shear strain in the Central Walker Lane, western North

America: Constraints from dense GPS measurements. *Earth and Planetary Science Letters*, *440*, 169 – 177. doi:10.1016/j.epsl.2016.01.015.

Cervelli, P. F. (2013). Analytical Expressions for Deformation from an Arbitrarily Oriented Spheroid in a Half-Space. In *AGU Fall Meeting Abstracts* (pp. V44C–06). volume 2013.

Chan, K., Lee, T.-W., & Sejnowski, T. J. (2003). Variational Bayesian Learning of ICA with Missing Data. *Neural Computation*, *15*, 1991–2011. doi:10.1162/08997660360675116.

Chang, W.-L., Smith, R. B., Farrell, J., & Puskas, C. M. (2010). An extraordinary episode of Yellowstone caldera uplift, 2004–2010, from GPS and InSAR observations. *Geophysical Research Letters*, *37*. doi:10.1029/2010GL045451.

Cheng, C. H., & Johnston, D. H. (1981). Dynamic and static moduli. *Geophysical Research Letters*, *8*, 39–42. doi:https://doi.org/10.1029/GL008i001p00039.

Choudrey, R. A., & Roberts, S. J. (2003). Variational mixture of Bayesian independent component analyzers. *Neural computation*, *15*, 213–252. doi:10.1162/089976603321043766.

D'Agostino, N., Silverii, F., Amoroso, O., Convertito, V., Fiorillo, F., Ventafridda, G., & Zollo, A. (2018). Crustal Deformation and Seismicity Modulated by Groundwater Recharge of Karst Aquifers. *Geophysical Research Letters*, *45*, 12,253–12,262. doi:10.1029/2018GL079794.

Dawson, P. B., Evans, J. R., & Iyer, H. M. (1990). Teleseismic tomography of the compressional wave velocity structure beneath the Long Valley Region, California. *Journal of Geophysical Research: Solid Earth*, *95*, 11021–11050. doi:10.1029/JB095iB07p11021.

Drouin, V., Heki, K., Sigmundsson, F., Hreinsdóttir, S., & Ófeigsson, B. G. (2016). Constraints on seasonal load variations and regional rigidity from

continuous GPS measurements in Iceland, 1997–2014. *Geophysical Journal International*, *205*, 1843–1858. doi:10.1093/gji/ggw122.

Farr, T. G., Rosen, P. A., Caro, E., Crippen, R., Duren, R., Hensley, S., Kobrick, M., Paller, M., Rodriguez, E., Roth, L., Seal, D., Shaffer, S., Shimada, J., Umland, J., Werner, M., Oskin, M., Burbank, D., & Alsdorf, D. (2007). The Shuttle Radar Topography Mission. *Reviews of Geophysics*, *45*. doi:10.1029/2005RG000183.

Feng, L., & Newman, A. V. (2009). Constraints on continued episodic inflation at Long Valley Caldera, based on seismic and geodetic observations. *Journal of Geophysical Research: Solid Earth*, *114*. doi:10.1029/2008JB006240.

Fialko, Y., Simons, M., & Khazan, Y. (2001). Finite source modelling of magmatic unrest in Socorro, New Mexico, and Long Valley, California. *Geophysical Journal International*, *146*, 191–200. doi:10.1046/j.1365-246X.2001.00453.x.

Flinders, A. F., Shelly, D. R., Dawson, P. B., Hill, D. P., Tripoli, B., & Shen, Y. (2018). Seismic evidence for significant melt beneath the Long Valley Caldera, California, USA. *Geology*, *46*, 799–802. doi:10.1130/G45094.1.

Frassetto, A. M., Zandt, G., Gilbert, H., Owens, T. J., & Jones, C. H. (2011). Structure of the Sierra Nevada from receiver functions and implications for lithospheric foundering. *Geosphere*, *7*, 898–921. doi:10.1130/GES00570.1.

Gardner, G., Gardner, L., & Gregory, A. (1974). Formation velocity and density—the diagnostic basics for stratigraphic traps. *Geophysics*, *39*, 770–780. doi:10.1190/1.1440465.

Gualandi, A., Perfettini, H., Radiguet, M., Cotte, N., & Kostoglodov, V. (2017). GPS deformation related to the Mw 7.3, 2014, Papanoa earthquake (Mexico) reveals the aseismic behavior of the Guerrero seismic gap. *Geophysical Research Letters*, *44*, 6039–6047. doi:10.1002/2017GL072913.

Gualandi, A., Serpelloni, E., & Belardinelli, M. (2016). Blind source separation problem in GPS time series. *Journal of Geodesy*, *90*, 323–341. doi:10.1007/s00190-015-0875-4.

Hammond, W., Kreemer, C., Zaliapin, I., & Blewitt, G. (2019). Drought-triggered magmatic inflation, crustal strain and seismicity near the Long Valley Caldera, Central Walker Lane. *Journal of Geophysical Research: Solid Earth*, *124*, 6072–6091. doi:10.1029/2019JB017354.

Hammond, W. C., Blewitt, G., & Kreemer, C. (2016). GPS imaging of vertical land motion in California and Nevada: Implications for Sierra Nevada uplift. *Journal of Geophysical Research: Solid Earth*, *121*, 7681–7703. doi:10.1002/2016JB013458.

Hildreth, W. (2017). Fluid-driven uplift at Long Valley Caldera, California: geologic perspectives. *Journal of Volcanology and Geothermal Research*, *341*, 269–286. doi:10.1016/j.jvolgeores.2017.06.010.

Hill, D., Montgomery-Brown, E., Shelly, D., Flinders, A., & Prejean, S. (2020). Post-1978 tumescence at Long Valley Caldera, California: A geophysical perspective. *Journal of Volcanology and Geothermal Research*, *400*, 106900. doi:10.1016/j.jvolgeores.2020.106900.

Hu, X., & Bürgmann, R. (2020). Aquifer deformation and active faulting in Salt Lake Valley, Utah, USA. *Earth and Planetary Science Letters*, *547*, 116471. doi:10.1016/j.epsl.2020.116471.

Ji, K. H., Herring, T. A., & Llenos, A. L. (2013). Near real-time monitoring of volcanic surface deformation from GPS measurements at Long Valley Caldera, California. *Geophysical Research Letters*, *40*, 1054–1058. doi:10.1029/2017JB015420.

Julian, B., & Sipkin, S. (1985). Earthquake processes in the Long Valley caldera area, California. *Journal of Geophysical Research*, *90*, 11,155–11,169. doi:10.1029/JB090iB13p11155.

Kreemer, C., & Zaliapin, I. (2018). Spatiotemporal Correlation Between Seasonal Variations in Seismicity and Horizontal Dilatational Strain in California. *Geophysical Research Letters*, *45*, 9559–9568. doi:10.1029/2018GL079536.

Landerer, F. W., Flechtner, F. M., Save, H., Webb, F. H., Bandikova, T., Bertiger, W. I., Bettadpur, S. V., Byun, S. H., Dahle, C., Dobslaw, H., Fahnestock, E., Harvey, N., Kang, Z., Kruizinga, G. L. H., Loomis, B. D., McCullough, C., Murböck, M., Nagel, P., Paik, M., Pie, N., Poole, S., Strekalov, D., Tamisiea, M. E., Wang, F., Watkins, M. M., Wen, H.-Y., Wiese, D. N., & Yuan, D.-N. (2020). Extending the Global Mass Change Data Record: GRACE Follow-On Instrument and Science Data Performance. *Geophysical Research Letters*, *47*, e2020GL088306.

Langbein, J. (2003). Deformation of the Long Valley Caldera, California: inferences from measurements from 1988 to 2001. *Journal of Volcanology and Geothermal Research*, *127*, 247–267. doi:10.1016/S0377-0273(03)00172-0.

Langbein, J., Dzurisin, D., Marshall, G., Stein, R., & Rundle, J. (1995). Shallow and peripheral volcanic sources of inflation revealed by modeling two-color geodimeter and leveling data from Long Valley Caldera, California, 1988–1992. *Journal of Geophysical Research: Solid Earth*, *100*, 12487–12495. doi:10.1029/95JB01052.

Lin, Y.-n. N., Kositsky, A. P., & Avouac, J.-P. (2010). PCAIM joint inversion of InSAR and ground-based geodetic time series: Application to monitoring magmatic inflation beneath the Long Valley Caldera. *Geophysical Research Letters*, *37*. doi:10.1029/2010GL045769.

Liu, Z., Dong, D., & Lundgren, P. (2011). Constraints on time-dependent volcanic source models at Long Valley Caldera from 1996 to 2009 using InSAR and geodetic measurements. *Geophysical Journal International*, *187*, 1283–1300. doi:10.1111/j.1365-246X.2011.05214.x.

Long, S. M., & Grosfils, E. B. (2009). Modeling the effect of layered volcanic material on magma reservoir failure and associated deformation, with application

to Long Valley caldera, California. *Journal of Volcanology and Geothermal Research*, *186*, 349–360. doi:10.1016/j.jvolgeores.2009.05.021.

Magni, V., Battaglia, M., Tizzani, P., Manconi, A., & Walter, T. (2008). Axial symmetric crustal deformation model for Long Valley Caldera, California. In *Excerpt from Proceedings of the COMSOL Conference 2008*. Hannover.

Marshall, G. A., Langbein, J., Stein, R. S., Lisowski, M., & Svarc, J. (1997). Inflation of Long Valley Caldera, California, Basin and Range Strain, and possible mono craters dike opening from 1990–94 GPS surveys. *Geophysical Research Letters*, *24*, 1003–1006. doi:10.1029/97GL00885.

Masterlark, T., Donovan, T., Feigl, K. L., Haney, M., Thurber, C. H., & Tung, S. (2016). Volcano deformation source parameters estimated from InSAR: Sensitivities to uncertainties in seismic tomography. *Journal of Geophysical Research: Solid Earth*, *121*, 3002–3016. doi:https://doi.org/10.1002/2015JB012656.

McMechan, G. A., Luetgert, J. H., & Mooney, W. D. (1985). Imaging of earthquake sources in Long Valley Caldera, California, 1983. *Bulletin of the Seismological Society of America*, *75*, 1005–1020.

Montgomery-Brown, E., Shelly, D., & Hsieh, P. (2019). Snowmelt-triggered earthquake swarms at the margin of Long Valley Caldera, California. *Geophysical Research Letters*, *46*, 3698–3705. doi:10.1029/2019GL082254.

Montgomery-Brown, E., Wicks, C., Cervelli, P. F., Langbein, J. O., Svarc, J. L., Shelly, D. R., Hill, D. P., & Lisowski, M. (2015). Renewed inflation of Long Valley Caldera, California (2011 to 2014). *Geophysical Research Letters*, *42*, 5250–5257. doi:10.1002/2015GL064338.

Murray, J. R., & Svarc, J. (2017). Global Positioning System data collection, processing, and analysis conducted by the US Geological Survey Earthquake Hazards Program. *Seismological Research Letters*, *88*, 916–925. doi:10.1785/0220160204.

Nelder, J. A., & Mead, R. (1965). A Simplex Method for Function Minimization. *The Computer Journal*, *7*, 308–313. doi:10.1093/comjnl/7.4.308.

Newman, A. V., Dixon, T. H., & Gourmelen, N. (2006). A four-dimensional viscoelastic deformation model for Long Valley Caldera, California, between 1995 and 2000. *Journal of volcanology and geothermal research*, *150*, 244–269. doi:10.1016/j.jvolgeores.2005.07.017.

Nikkhoo, M., Walter, T. R., Lundgren, P. R., & Prats-Iraola, P. (2017). Compound dislocation models (CDMs) for volcano deformation analyses. *Geophysical Journal International*, *208*, 877–894. doi:doi.org/10.1093/gji/ggw427.

Peacock, J. R., Mangan, M. T., McPhee, D., & Ponce, D. A. (2015). Imaging the magmatic system of Mono Basin, California, with magnetotellurics in three dimensions. *Journal of Geophysical Research: Solid Earth*, *120*, 7273–7289. doi:10.1002/2015JB012071.

Peacock, J. R., Mangan, M. T., McPhee, D., & Wannamaker, P. E. (2016). Three-dimensional electrical resistivity model of the hydrothermal system in Long Valley Caldera, California, from magnetotellurics. *Geophysical Research Letters*, *43*, 7953–7962. doi:10.1002/2016GL069263.

Pepe, S., Tizzani, P., & Manconi, A. (2010). Numerical inversion of surface deformation at Long Valley Caldera (California) by using 3D mechanical models. In *Excerpt from the Proceedings of the COMSOL Conference 2010*.

Pintori, F., Serpelloni, E., Longuevergne, L., Garcia, A., Faenza, L., D'Alberto, L., Gualandi, A., & Belardinelli, M. E. (2021). Mechanical Response of Shallow Crust to Groundwater Storage Variations: Inferences from Deformation and Seismic Observations in the Eastern Southern Alps, Italy. *Journal of Geophysical Research: Solid Earth*, . doi:10.1029/2020JB020586.

Prudencio, J., & Manga, M. (2019). 3-D seismic attenuation structure of Long Valley caldera: looking for melt bodies in the shallow crust. *Geophysical Journal International*, *220*, 1677–1686. doi:10.1093/gji/ggz543.

Riddick, S. N., & Schmidt, D. A. (2011). Time-dependent changes in volcanic inflation rate near Three Sisters, Oregon, revealed by InSAR. *Geochemistry, Geophysics, Geosystems*, *12*. doi:10.1029/2011GC003826.

Ruppert, S., Fliedner, M. M., & Zandt, G. (1998). Thin crust and active upper mantle beneath the Southern Sierra Nevada in the western United States. *Tectonophysics*, *286*, 237–252. doi:10.1016/S0040-1951(97)00268-0.

Savage, J. C. (1988). Principal Component Analysis of Geodetically Measured Deformation in Long Valley Caldera, Eastern California, 1983–1987. *Journal of Geophysical Research: Solid Earth*, *93*, 13297–13305. doi:10.1029/JB093iB11p13297.

Serpelloni, E., Pintori, F., Gualandi, A., Scoccimarro, E., Cavaliere, A., Anderlini, L., Belardinelli, M. E., & Todesco, M. (2018). Hydrologically Induced Karst Deformation: Insights From GPS Measurements in the Adria-Eurasia Plate Boundary Zone. *Journal of Geophysical Research: Solid Earth*, *123*, 4413–4430. doi:10.1002/2017JB015252.

Shelly, D. R., Ellsworth, W. L., & Hill, D. P. (2016). Fluid-faulting evolution in high definition: Connecting fault structure and frequency-magnitude variations during the 2014 Long Valley Caldera, California, earthquake swarm. *Journal of Geophysical Research: Solid Earth*, *121*, 1776–1795. doi:10.1002/2015JB012719.

Shelly, D. R., Taira, T., Prejean, S. G., Hill, D. P., & Dreger, D. S. (2015). Fluid-faulting interactions: Fracture-mesh and fault-valve behavior in the February 2014 Mammoth Mountain, California, earthquake swarm. *Geophysical Research Letters*, *42*, 5803–5812. doi:10.1002/2015GL064325.

Silverii, F., Montgomery-Brown, E. K., Borsa, A. A., & Barbour, A. J. (2020). Hydrologically Induced Deformation in Long Valley Caldera and Adjacent Sierra Nevada. *Journal of Geophysical Research: Solid Earth*, *125*, e2020JB019495. doi:10.1029/2020JB019495.

Tiampo, K., Rundle, J., Fernandez, J., & Langbein, J. (2000). Spherical and ellipsoidal volcanic sources at Long Valley caldera, California, using a genetic algorithm inversion technique. *Journal of Volcanology and Geothermal Research*, *102*, 189 – 206. doi:10.1016/S0377-0273(00)00185-2.

Walwer, D., Calais, E., & Ghil, M. (2016). Data-adaptive detection of transient deformation in geodetic networks. *Journal of Geophysical Research: Solid Earth*, *121*, 2129–2152. doi:10.1002/2015JB012424.

Wessel, P., Smith, W. H., Scharroo, R., Luis, J., & Wobbe, F. (2013). Generic mapping tools: improved version released. *Eos, Transactions American Geophysical Union*, *94*, 409–410. doi:10.1002/2013EO450001.

Supporting material for "The 2011-2019 Long Valley Caldera inflation: new insights from separation of superimposed geodetic signals and 3D modeling"

F. Silverii[a,b,*], F. Pulvirenti[c], E. K. Montgomery-Brown[d], A. A. Borsa[b], W. R. Neely[b]

[a] *German Research Centre for Geosciences (GFZ), Potsdam, Germany*
[b] *Scripps institution of Oceanography, University of California San Diego, La Jolla, California, USA*
[c] *Nanjing University of Information Science and Technology, Ningliu Road, Nanjing-China*
[d] *Cascades Volcano Observatory, United States Geological Survey, Vancouver, Washington, USA*

Contents of this file

1. Text S1 to S3
2. Figures S1 to S13
3. Table S1

*Corresponding author
Email address: silverii@gfz-potsdam.de (F. Silverii)

Text S1. Estimation of surface deformation from GRACE data

For each GNSS station in our study area, we estimated three components (North/East/Up) of solid earth elastic displacements from hydrological loading. Our input loads were taken from time-series of global terrestrial water storage change from the joint NASA/GFZ Gravity Recovery and Climate Experiment (GRACE) and GRACE Follow-On (GRACE-FO) missions (Wahr et al., 1998; Landerer et al., 2020). We used the Center for Space Research (CSR) RL06 data product, which provides quasi-monthly estimates of water storage on a regular 0.5-degree grid (Save et al., 2016; Save, 2020). The CSR solution includes 180 epochs between April 2002 and December 2019, which reflects a number of missing monthly epochs and an 11-month gap between missions beginning July 2017. We interpolated the CSR GRACE/GRACE-FO water storage to daily GNSS epochs using cubic spline interpolation.

To forward-model load displacements at the GNSS station locations, we used the open-source SPOTL package (Agnew, 1997), which calculates elastic displacements from surface loads on a spherical earth. We assumed that the Earth's structure follows the Gutenberg-Bullen Model A average Earth reference model and defined displacements relative to Earth's center of mass. We used the interpolated GRACE/GRACE-FO gridded water storage observations as input into SPOTL and obtained daily displacement estimates at each station. Because of the GRACE monthly resolution and the cubic spline interpolation used, these daily displacements contain negligible variance at periods shorter than $\approx$2 months.

In its application to the Long Valley study area, the GRACE/GRACE-FO dataset provides good estimates of displacements from distant loads, but it is does not perform as well for large nearby loads in the Sierra Nevada (Figure 4 in the main text). This is because GRACE has a spatial resolution of 400 km (Luthcke et al., 2013), which results in the delocalization of large loads nearby

Sierra Nevada. Since load displacements are an inverse function of distance to the load, GNSS displacement estimates are underestimated.

Text S2. vbICA decomposition including only horizontal components and excluding sites in LVC South Moat

As discussed in the main text (Section 3.1), we ran an additional vbICA decomposition test in order to evaluate the effect on the decomposition of the GNSS sites and components that are potentially more affected by non-volcanic transient processes. In particular, the GNSS sites located in the Long Valley Caldera (LVC) South Moat (that are also the ones affected by the highest horizontals seasonal signal, (Silverii et al., 2020)) show a higher variation of the horizontal velocity in time (up to ≈10 mm/yr of variation between the T1 and T2 intervals, black arrows in Figure 5 – left column – in the main text). The vertical component, on the other hand, is known to be highly affected by the hydrological loading and its spatio-temporal variation (Argus et al., 2017), and shows a variation up to ≈17 mm/yr between the T1 and T2 intervals (black arrows in Figure 5 – right column – in the main text).

We therefore ran a vbICA decomposition test considering only the horizontal components and excluding the sites located in LVC south of RDOM (CA99, HOTK, KNOL, LINC, MINS, MWTP, P628, P630, P631, P639, P642, P643, P644, SHRC, TILC, WATC). The results for the 4 Independent Components (ICs) - as determined through the ARD and NFE criteria (see Section 2 in the main text) - are represented in Figure S6. As for the case with all stations and both horizontals and vertical time-series (hereafter "all-sites and all-components decomposition", Figure 3 in the main text), the first IC is mostly related to the caldera inflation centered in the resurgent dome, while the remaining components are mostly associated with transient (hydrological) signals at different time scales and horizontal Common Mode Error (CME).

Focusing first on the last three ICs, we observe that the seasonal signal (IC3) presents similar spatial features to the all-sites and all-components decompo-

sition results, with higher magnitude at the sites on the Sierra Nevada Range (SNR) edge. The multiyear deformation is less clearly separated and appears in both IC2 and IC4, mixed with the horizontal CME – this is probably because of its lower magnitude due to the exclusion of the South Moat sites and of the vertical time-series. However, some clear feature stands out like a peculiar behavior of the sites at the LVC center and eastern SNR edge.

IC1 shows a spatial and temporal pattern that is very similar to the one of the all-sites and all-components decomposition case (IC1 in Figure 3 of the main text), but with a less pronounced slope variation during the recent inflation episode starting in 2011.75. Analogously to the all-sites and all-components decomposition case (Section 3 in the main text), for each site we estimated the velocities in the T1 (2011.75–2014.84) and T2 (2014.84–2018.83) intervals from the IC1-reconstructed (horizontal) time-series. Figure S7 shows the comparison between the velocities distribution in the two cases: in T1 the all-sites and all-components decomposition case results (black arrows) show lower velocity values, whereas the opposite occurs in T2. The differences between the velocity values in the two cases reach the highest values (up to ≈0.6 mm/yr in T1 and ≈0.9 mm/yr in T2) at the sites north of the resurgent dome (BALD, DDMN, KRAC, P638, location in Figure 1 of the main text), but fall within the velocity uncertainties.

Text S3. Inflation forward models: assessing effect of topography and material heterogeneity

In order to assess the effect of topography and material heterogeneities on the inflation-related deformation at surface, we performed a series of forward models in different model setups: flat surface or with topography, homogeneous and heterogeneous material properties.

We assumed an ellipsoidal source with parameters compatible with the best-fit values estimated for the most recent inflation episode (from 2011 to 2015) by Montgomery-Brown et al. (2015). The ellipsoid is vertical (dip angle = 0°) with

0° strike, located beneath the resurgent dome at E_x = 8000 m and E_y = 20400 m, with horizontal semi-axes $E_a = E_b$ = 1700 m, vertical semi-axis E_c = 3000 m, and pressure change of ΔP = 5 MPa/yr. The source vertical position (from z=0 m, at sea level, to the ellipsoid center, z positive upward) is E_z = -6000 m b.s.l.. Note that in the model with flat surface (i.e. without topography) the free surface is located at 2300 m above sea level in order to compensate for the average elevation in the examined area.

The heterogeneous and homogeneous material properties are the same as explained in Section 4.1 of the main text.

The velocity inversion results (Section 5 of the main text) consistently provide a higher value of the E_a semi-axis compared to E_b, with a ratio of $E_a/E_b \approx 1.1$ (E_a being oriented along the x-axis and E_b along the y-axis, as represented in Figure 6c of the main text). We therefore implemented an additional model to test the effect of this source asymmetry using ellipsoid axes values of E_a = 1783 m and E_b = 1621 m, so that the ellipsoid volume is consistent with the previous tests.

Figure S8 shows the results for every tested model (map view of the estimated velocities at the free surface), starting from the simple flat-homogeneous case (Figure S8a) and progressively adding complexities: topography (Figure S8b) and material heterogeneity (Figure S8c). Figure S8d and Figure S8e show the effect of an asymmetrical source respectively for the homogeneous and heterogeneous material cases. The results for the horizontal velocity magnitude are calculated from the velocities in x (i.e. East) and y (i.e. North) direction, respectively u and v, as $\sqrt{u^2 + v^2}$.

As expected, the results of the flat-homogeneous case show radial symmetry with maximum horizontal velocity (≈0.9 mm/yr) distributed at ≈15 km radius from the projected position of the ellipsoid center and maximum vertical velocity (≈15.5 mm/yr) centered at the ellipsoid center position. The comparison of Figure S8a and S8b shows a slight effect of the topography on the horizontal component (≈0.05 mm/yr difference for the assumed ΔP value, i.e. 5% of the maximum value) in a restricted area mostly on the southwest side of LVC,

where the topographic elevation is higher. Adding the material heterogeneity causes a clear southwest-northeast asymmetry in the horizontal response in a region within a ≈20 km radius (i.e. about twice the source depth from free surface, that is 8.3 km) around the source position, with lower values on the SNR side, where the material is stiffer (see Figure 6 in the main text). This velocity variation between the southwest and northeast sides goes up to ≈2 mm/yr, representing a decrease of ≈20% with respect to the flat homogeneous model in the southwest area and a widening of the maximum deformation area in the northeast. The vertical component shows some east-west asymmetry with the maximum deformation area slightly shifting towards east (≈2 km, i.e. about a quarter of the source depth) around the ellipsoid position.

The asymmetrical source causes an asymmetrical response in both horizontal and vertical components, with higher amplitudes south and north of the source (Figure S8d). When material heterogeneity is also included, an additional southwest-northeast asymmetry appears, with the horizontal response focusing on the north of the source and a more pronounced east-west asymmetry in the vertical deformation (Figure S8e).

Figure S9 shows the velocities expected at the LVC GNSS sites location. For the sake of figure clarity, we show only the results associated to the simplest case (flat and homogeneous, blue arrows), taken as reference, and the two most complex cases including topography, material heterogeneity (green arrows) and source asymmetry (red arrows). Being the GNSS network in this area fairly dense, the results show the effect of the previously highlighted asymmetries. As expected, the highest differences (up to 2 mm/yr horizontally and 1.5 mm/yr vertically, i.e. 20% and 10% of the maximum velocity values) affect the sites on the Southwest Moat (Figure S9b).

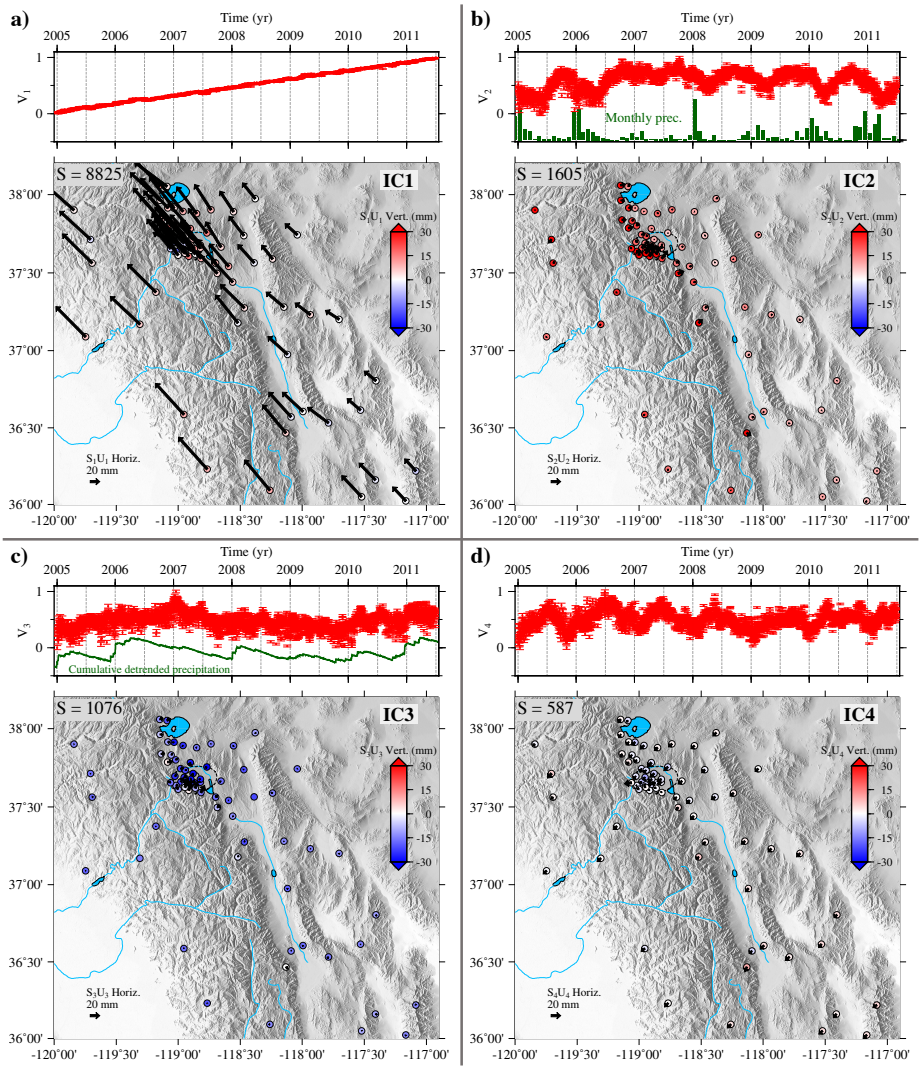

Figure S1: Results of the vbICA decomposition on time-series with long-term trend: each quadrant represents the temporal evolution (V, top) and map view of the spatial response ($S{\cdot}U$, bottom) of the 4 ICs. The weight S (mm) of each IC is indicated in the upper-left corner. The black arrows and the color coded circles respectively indicate the horizontal and vertical responses. The spatial response describes the directions along which the GNSS sites move and the arrow length and the circle color are proportional to the contribution of the specific component at every station. The green vertical bars (in IC2) and line (in IC3) represent respectively the monthly and cumulative detrended precipitation at Lee Vining (location in Figure 1 of the main text).

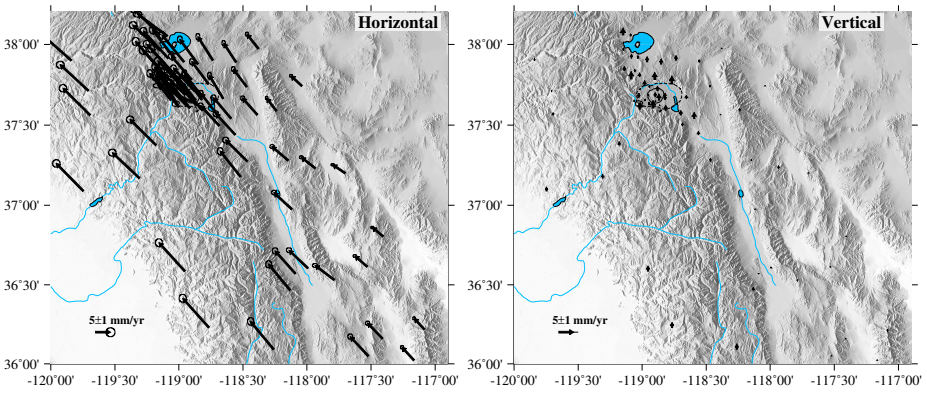

Figure S2: Spatial distribution of horizontal (left) and vertical (right) long-term trends estimated from the linear fit of time-series reconstructed from the IC1 component of Figure S1. Ellipses represent 68% CI.

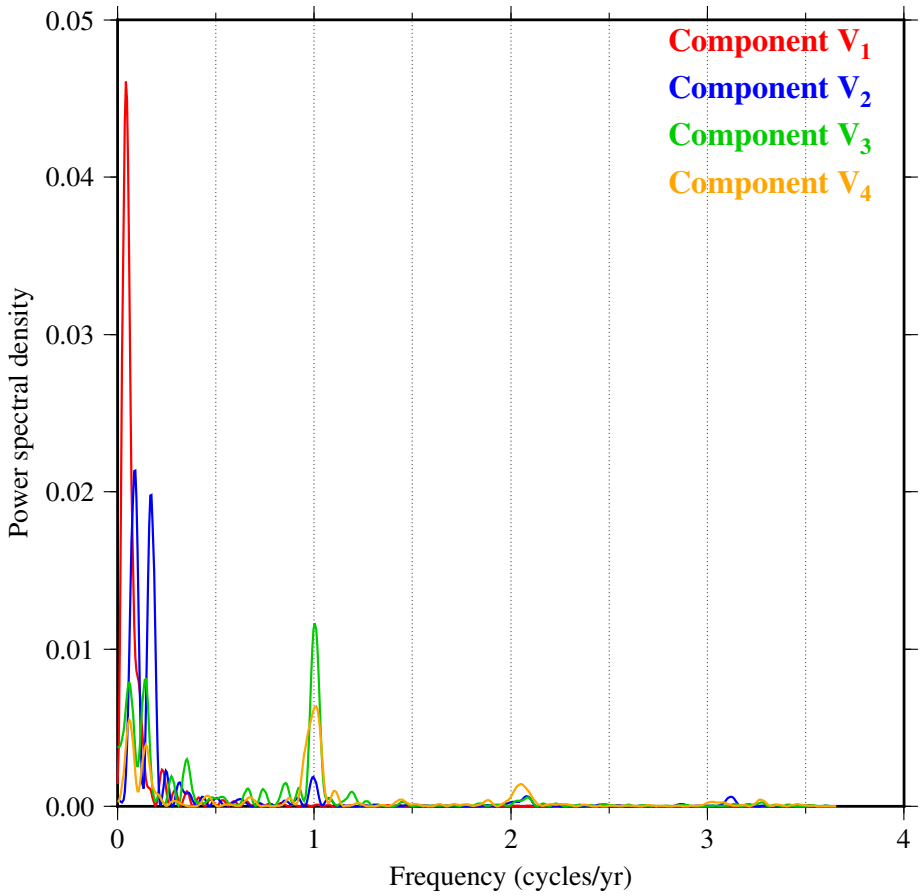

Figure S3: Power spectral density plot for the 4 temporal components of the vbICA decomposition shown in Figure 3 of the main text.

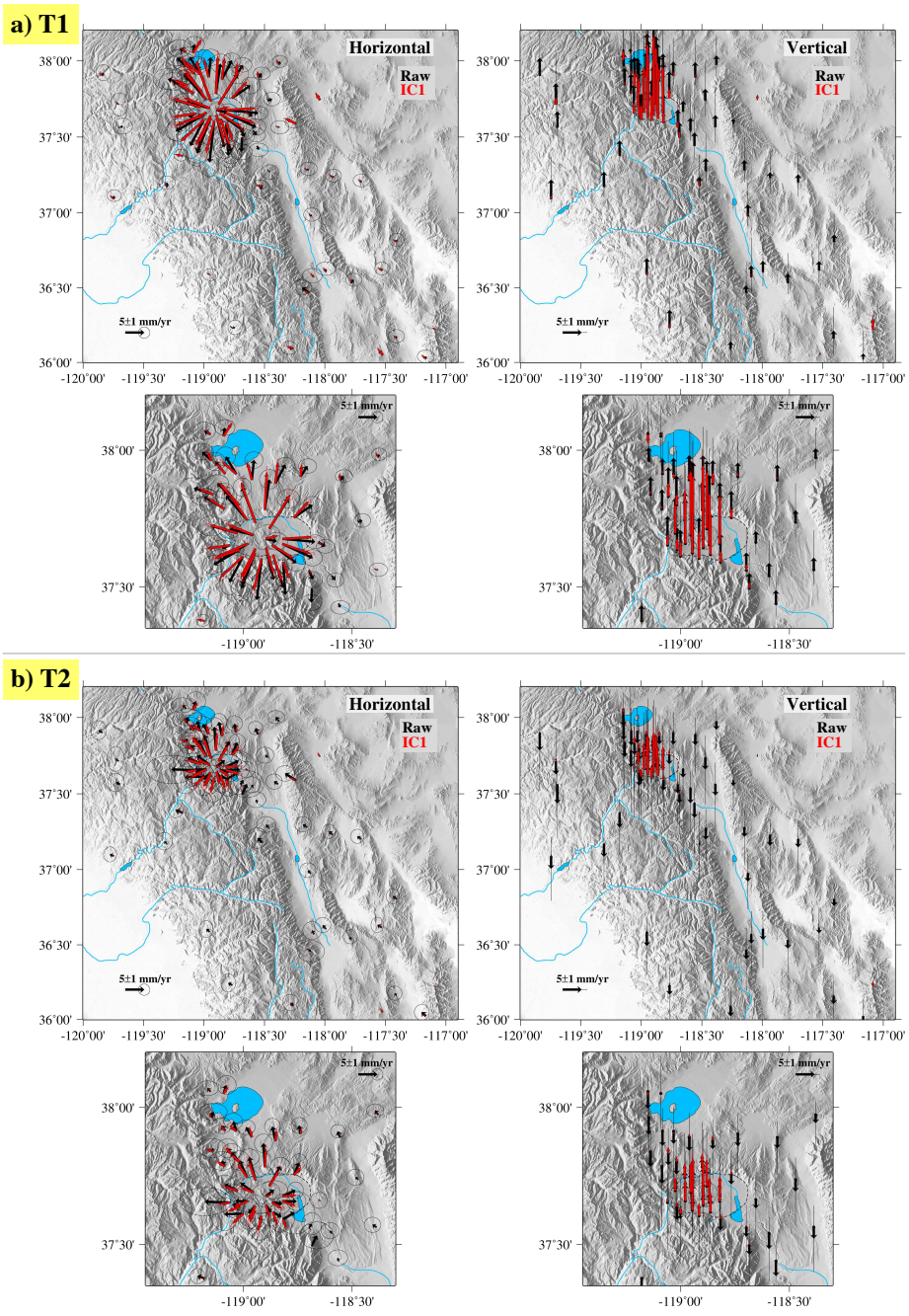

Figure S4: Maps of horizontal (left) and vertical (right) velocities estimated in the T1 (a) and T2 (b) time intervals. Same as Figure 5 in the main text, but before removing the horizontal CME. The black and red arrows (with 68% CI ellipses) correspond respectively to the raw and IC1-reconstructed time-series from which the velocities have been estimated. The smaller plots show enlarged maps of LVC area.

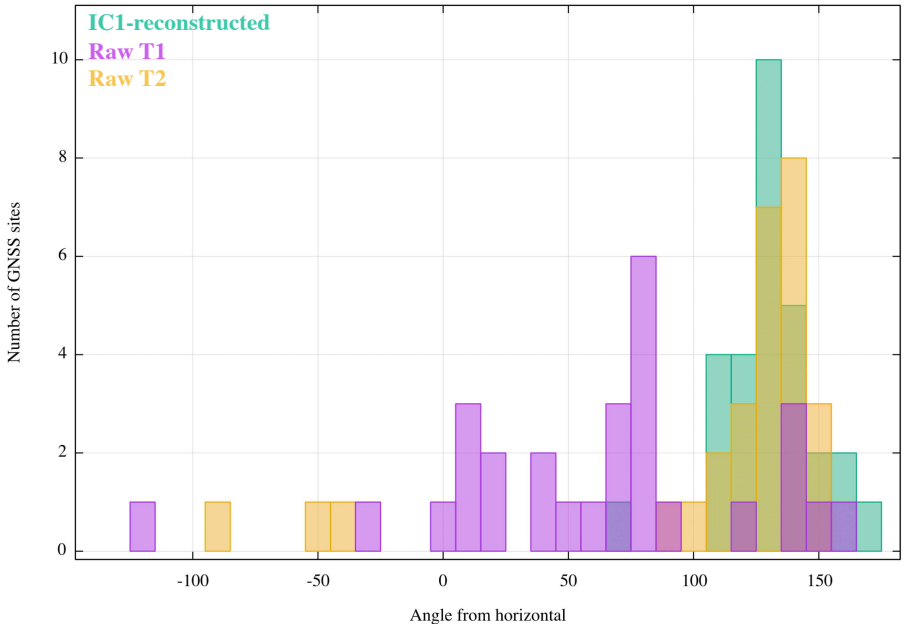

Figure S5: Distribution of horizontal velocities directions (as counterclockwise angle from the horizontal) for the far-field GNSS sites (i.e., at a radial distance >50 km from the resurgent dome) for the IC1-reconstructed and raw time-series in T1 and T2. The corresponding velocities spatial distribution is shown in Figure S4, left column.

.

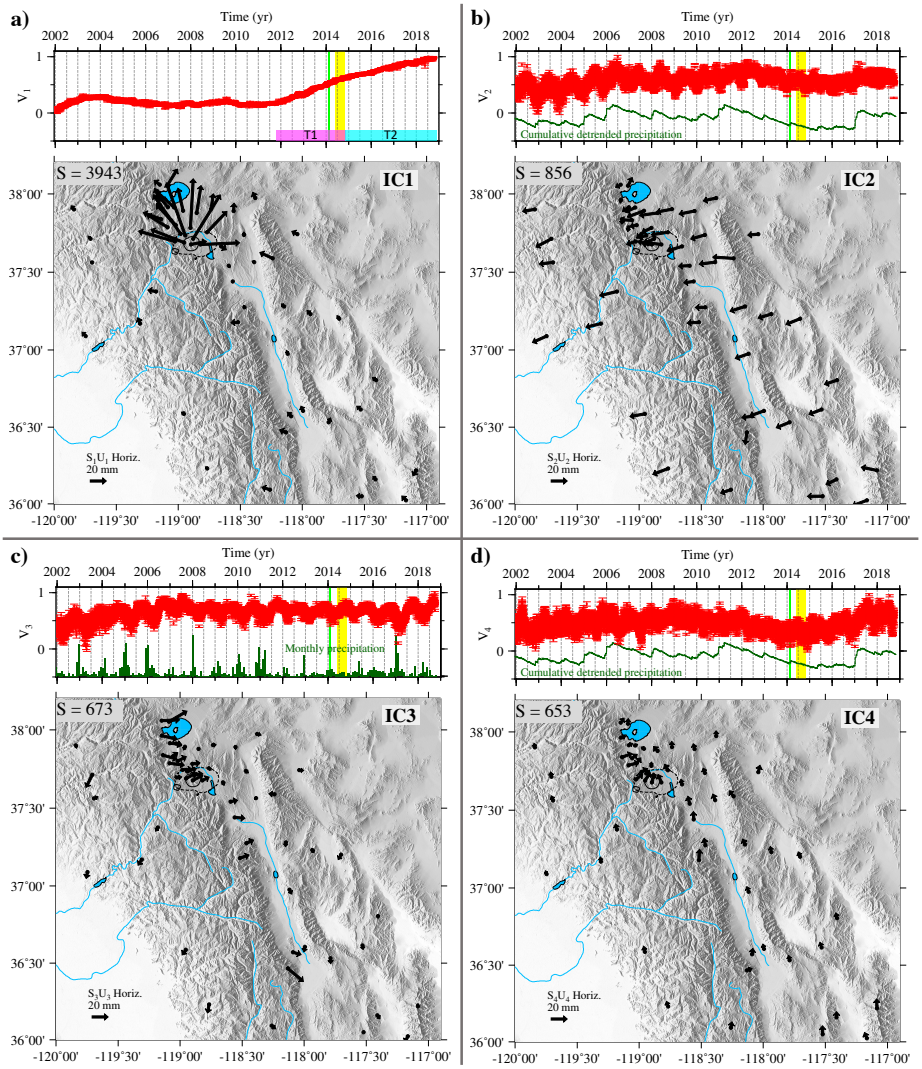

Figure S6: Results of the vbICA decomposition of only horizontal time-series, excluding the sites in the LVC South Moat. Each quadrant represents the temporal evolution (V, top – red dots with vertical bars representing one standard deviation errors) and map view of the spatial response ($S \cdot U$, bottom) of the 4 ICs. The weight S (mm) of each IC is indicated in the upper-left corner. The black arrows indicate the horizontal responses. The spatial response describes the directions along which the GNSS sites move and the arrow length and the circle color are proportional to the contribution of the specific component at every station. The green vertical bars (in IC3) and lines (in IC2 and IC4) represent respectively the monthly and cumulative detrended precipitation at Lee Vining. The green and yellow stripes show the time duration of the seismic swarms respectively in Mammoth Mountain and southeastern LVC.

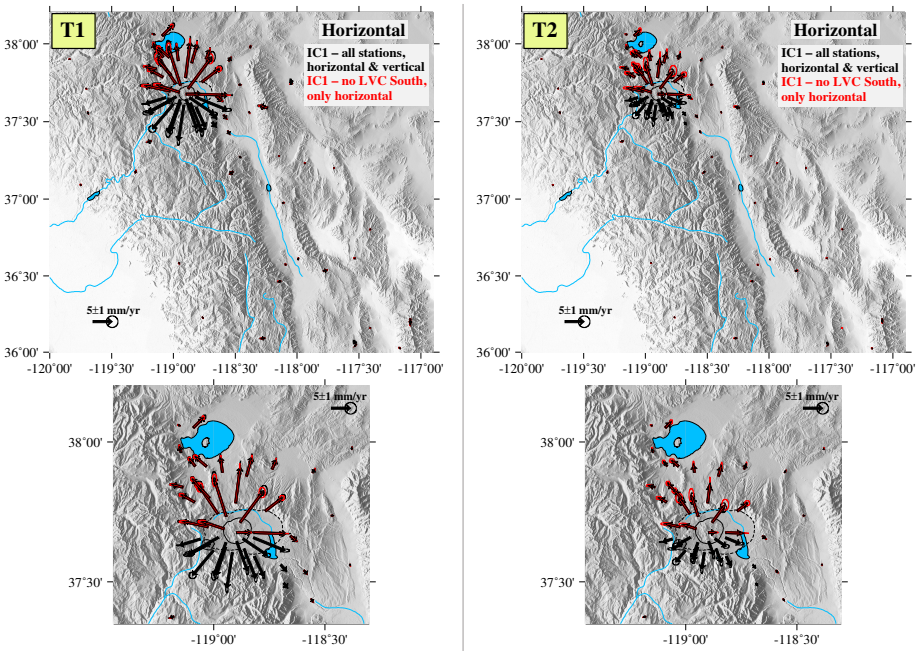

Figure S7: Maps of horizontal velocities in T1 and T2 time intervals estimated from the IC1-reconstructed time-series. The black and red arrows (with 68% CI ellipses) refer respectively to the results of decomposition using all-sites and all-components (horizontal and vertical) and the ones obtained excluding the sites in the LVC South Moat and using only the horizontal components. Smaller plots show enlarged maps of LVC area.

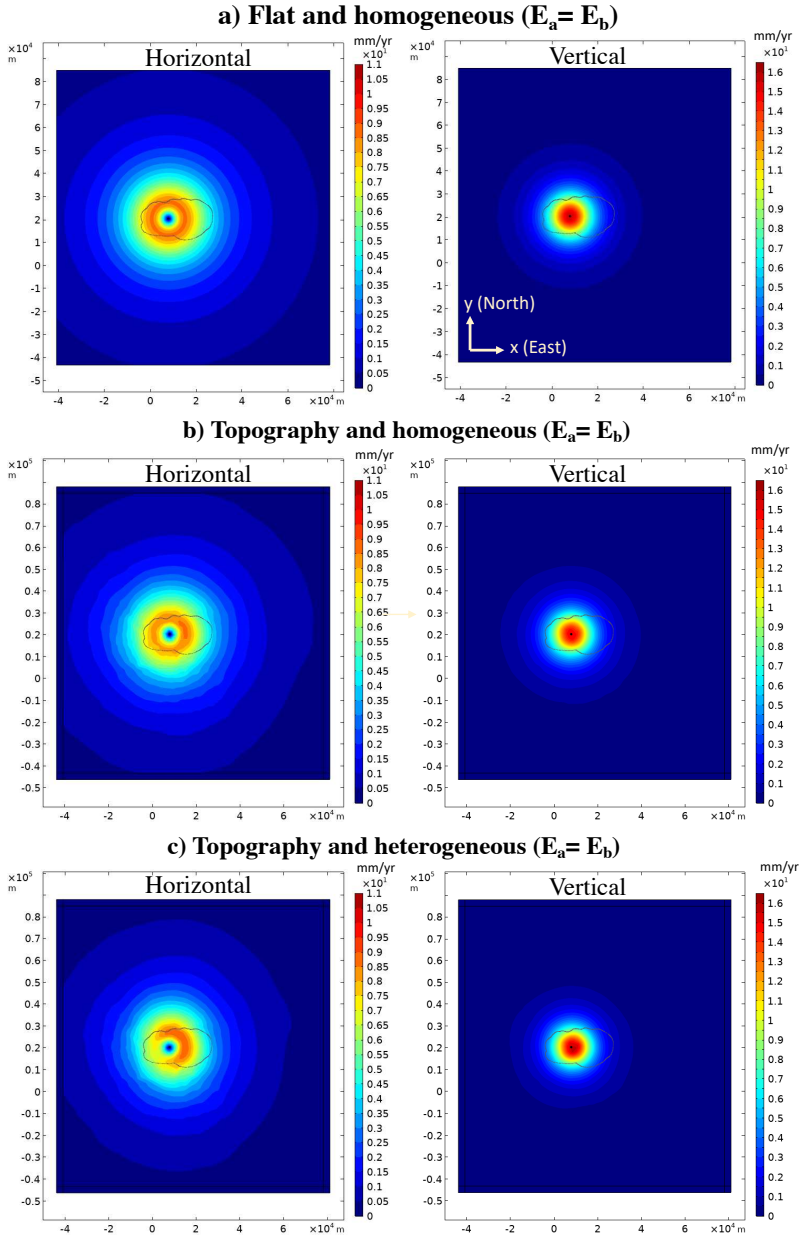

Figure S8: Forward-modelled horizontal and vertical velocity magnitude distribution at the free surface for a ellipsoid inflation of 5 MPa/yr for different model setups. The black circle indicates the projected horizontal ellipsoid center position, the grey line depicts the LVC contour. Note the different color scales for the horizontal and vertical components. E_a and E_b refer to the horizontal source ellipsoid axes oriented respectively along x and y (see Figure 6c in the main text). Continued on next page.

d) Topography and homogeneous (E_a=1.1·Eb)

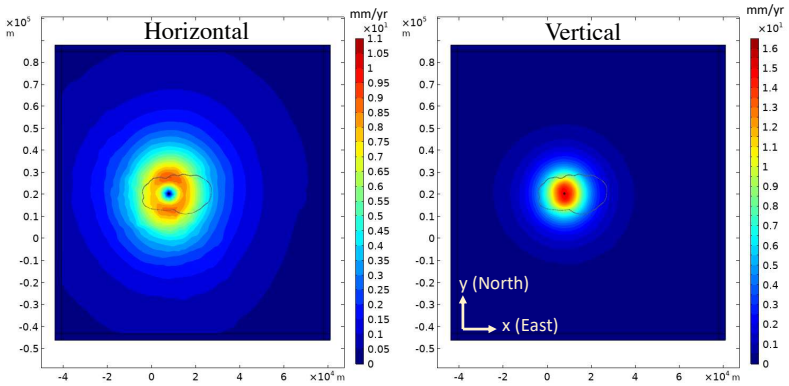

e) Topography and heterogeneous (E_a=1.1·Eb)

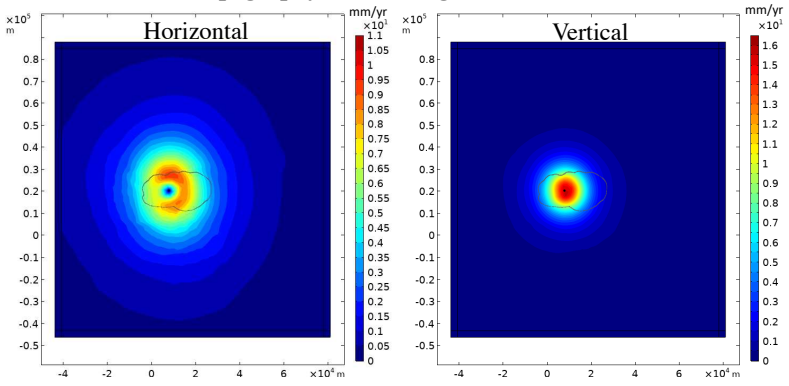

Figure S8: Continued from previous page.

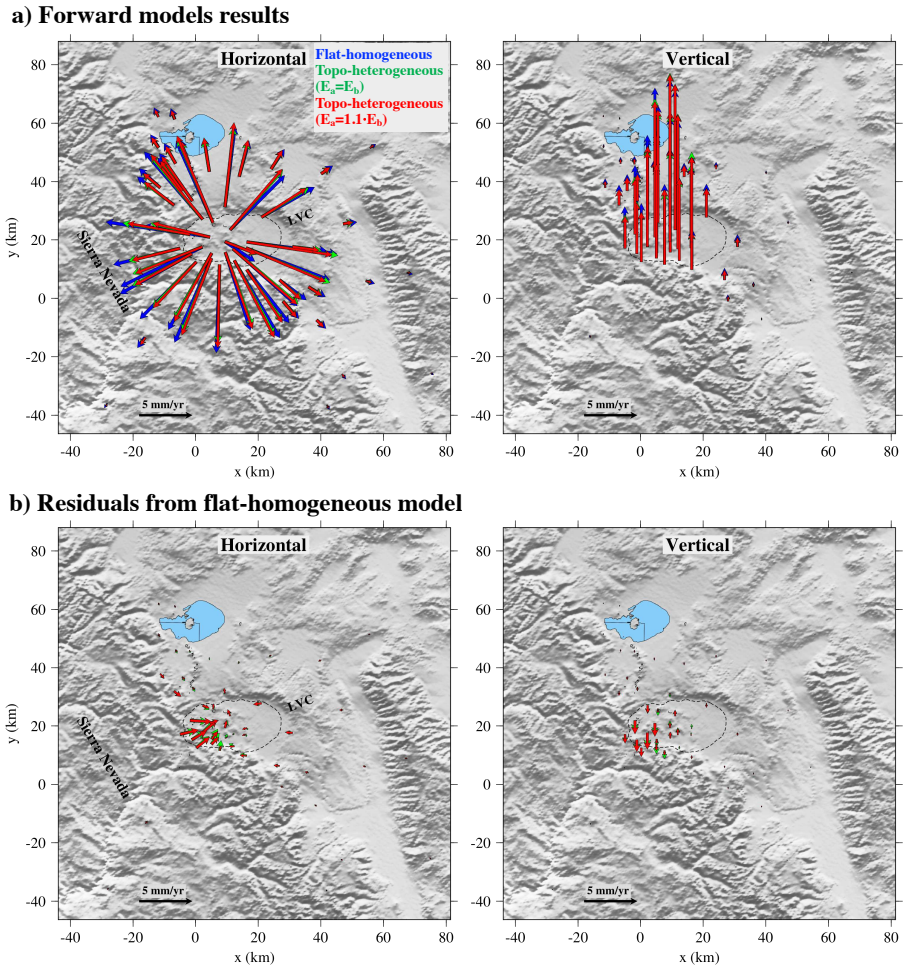

Figure S9: Forward modelled velocities (a) at the GNSS sites in LVC for the three different model setups listed in the legend and described in Section S3. The residuals (b) are obtained using the the flat-and-homogeneous model results as reference. E_a and E_b refer to the horizontal source ellipsoid axes oriented respectively along x and y (see Figure 6c in the main text).

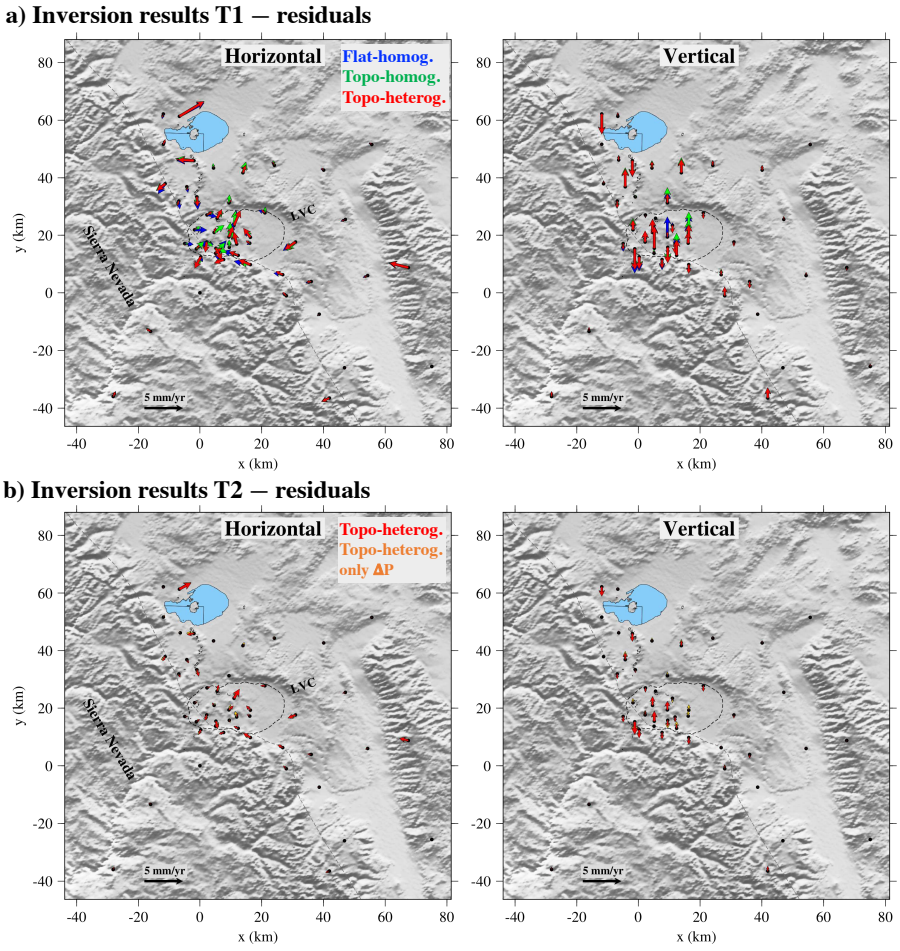

Figure S10: Velocity residuals (observed minus modeled) corresponding to the model results presented in Figure 7 of the main text.

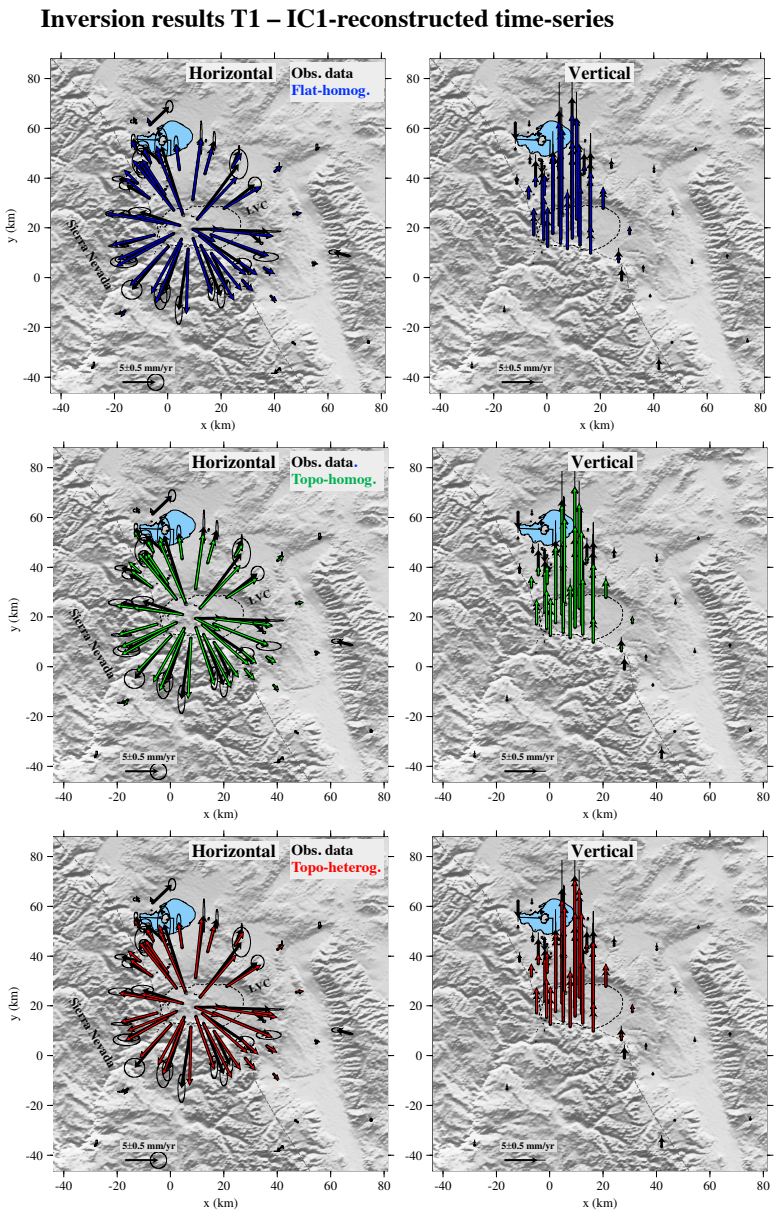

Figure S11: Same as Figure 7a of the main text, but showing separately the comparison between the observed (black arrows) and modeled (colored arrows) velocities for the different model settings for the IC1-reconstructed time-series case. Ellipses represent 95% CI.

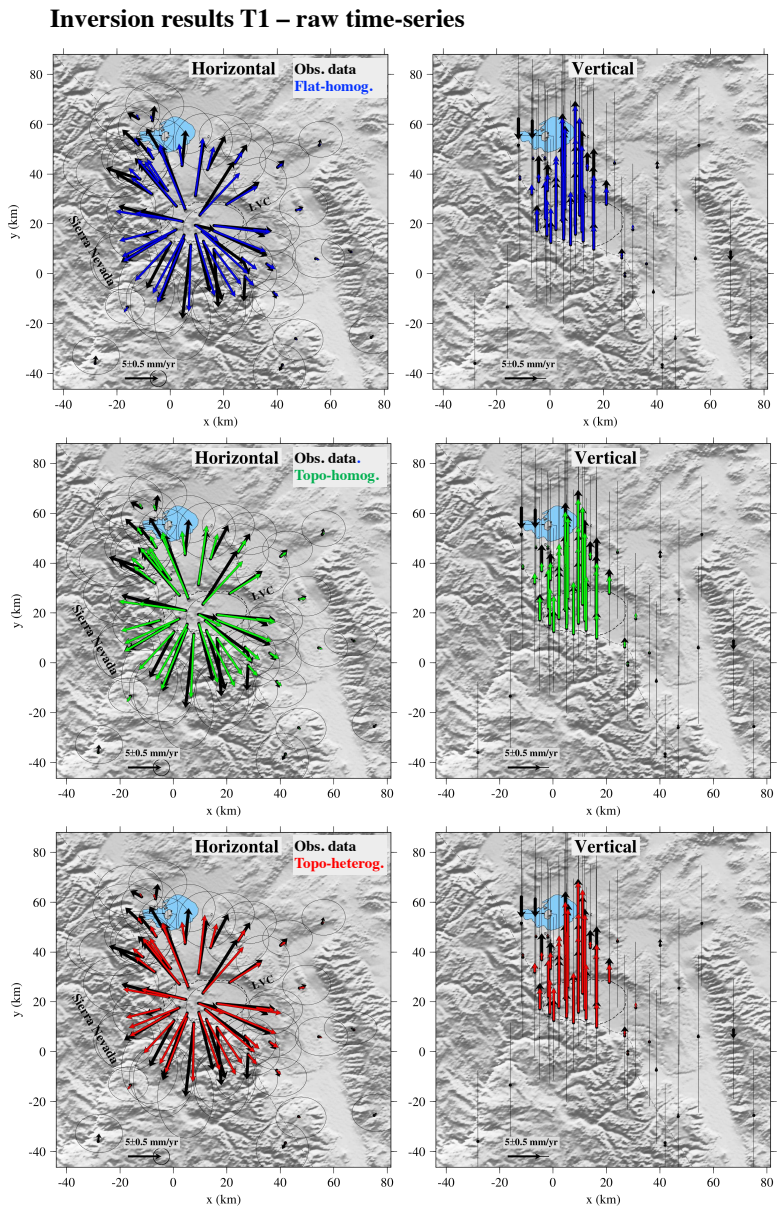

Figure S12: Same as Figure 8a of the main text, but showing separately the comparison between the observed (black arrows) and modeled (colored arrows) velocities for the different model settings for the raw time-series case. Ellipses represent 95% CI.

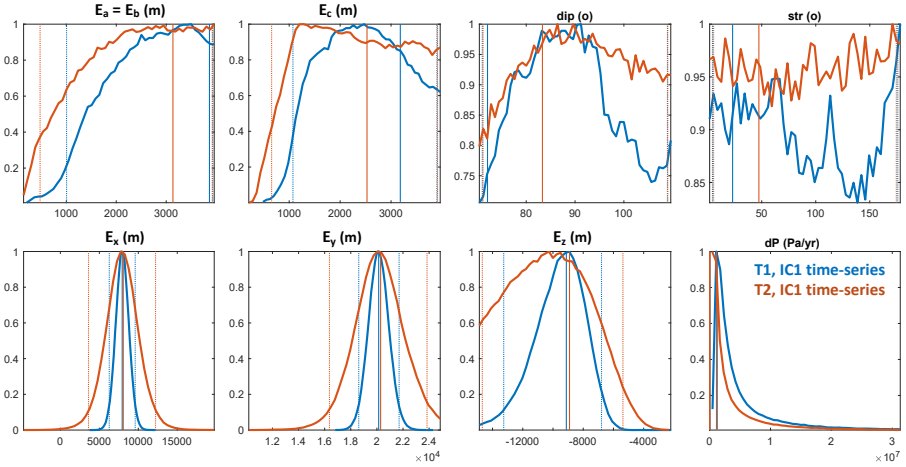

Figure S13: Posterior histograms for model parameters resulting from the MCMC analytical inversion model. The vertical lines indicate the preferred model (solid) and the 95% bounds (dotted) on the posterior distribution. Axis limits show the range of the uniform prior parameters distributions.

Table S1: GNSS stations name, location (longitude, latitude) and long-term velocities of the East (E), North (N) and Up (U) components with associated uncertainties.

Lon	**Lat**	V_E **(mm/yr)**	V_N **(mm/yr)**	V_U **(mm/yr)**	σV_E **(mm/yr)**	σV_N **(mm/yr)**	σV_U **(mm/yr)**	**Site ID**
-117.5219	36.0500	-6.047	6.506	0.233 7	0.552	0.593	0.021	ARGU
-118.9014	37.7834	-6.790	7.852	2.250	0.619	0.716	0.205	BALD
-118.8967	37.6446	-11.514	5.400	0.368	1.050	0.493	0.034	CA99
-118.9812	37.7442	-7.909	8.370	1.569	0.721	0.763	0.143	DDMN
-119.0906	38.0515	-9.979	7.366	0.704	0.910	0.672	0.064	DECH
-118.0393	37.7428	-3.687	3.410	0.139	0.336	0.311	0.013	DYER
-118.8213	37.6586	-6.019	7.996	1.221	0.549	0.729	0.111	HOTK
-118.9792	37.6591	-7.294	8.534	-0.395	0.665	0.778	0.036	KNOL
-118.8805	37.7133	-6.952	7.606	1.437	0.634	0.694	0.131	KRAC
-119.0173	37.6372	-6.560	10.356	-2.059	0.598	0.945	0.188	LINC
-119.0609	37.6538	-7.161	9.026	-0.494	0.653	0.823	0.045	MINS
-119.3093	37.1699	-9.041	8.519	1.137	0.825	0.777	0.104	MUSB
-118.9447	37.6405	-8.544	8.890	-0.561	0.779	0.811	0.051	MWTP
-117.5315	36.6143	-4.108	3.589	-0.222	0.375	0.327	0.020	P091
-117.4068	36.8042	-3.571	3.015	0.090	0.326	0.275	0.008	P092
-117.9941	36.6060	-6.302	5.961	0.235	0.575	0.544	0.021	P093
-117.7042	37.2008	-4.115	2.782	0.116	0.375	0.254	0.011	P094
-119.7061	37.7131	-9.449	8.717	-0.302	0.862	0.795	0.028	P245
-119.8402	37.9012	-9.410	8.344	0.540	0.858	0.761	0.049	P308
-118.5198	37.1776	-6.822	8.599	-0.029	0.622	0.784	0.003	P311
-117.1647	36.0225	-4.007	4.348	0.084	0.366	0.397	0.008	P463
-117.4100	36.1590	-5.029	5.223	-0.162	0.459	0.476	0.015	P464
-118.1324	36.4668	-7.179	8.655	0.866	0.655	0.789	0.079	P465
-117.7895	36.5313	-6.341	4.822	-0.361	0.578	0.440	0.033	P466
-118.0906	36.5702	-6.819	7.632	-0.107	0.622	0.696	0.010	P467
-118.1184	36.9757	-5.997	5.546	-0.127	0.547	0.506	0.012	P468
-117.9358	37.2314	-4.667	3.652	0.781	0.426	0.333	0.071	P469
-119.6945	37.5626	-9.069	8.981	0.699	0.827	0.819	0.064	P512
-118.7667	36.2314	-8.746	9.747	1.567	0.798	0.889	0.143	P571
-118.9546	36.5855	-8.674	9.575	1.636	0.791	0.873	0.149	P572
-118.2605	36.0931	-7.721	9.311	1.652	0.704	0.849	0.151	P573
-118.3785	37.9731	-3.890	4.890	0.161	0.355	0.446	0.015	P627

Continued on next page

Table S1 – continued from previous page

Lon	**Lat**	V_E **(mm/yr)**	V_N **(mm/yr)**	V_U **(mm/yr)**	σV_E **(mm/yr)**	σV_N **(mm/yr)**	σV_U **(mm/yr)**	**Station ID**
-119.1794	37.3759	-8.677	8.558	1.073	0.791	0.781	0.098	P629
-119.0004	37.6130	-8.006	10.354	0.388	0.730	0.944	0.035	P630
-118.9159	37.6053	-6.645	8.531	2.395	0.606	0.778	0.218	P631
-119.0861	37.7857	-8.409	9.659	2.369	0.767	0.881	0.216	P632
-119.0330	37.9135	-7.408	9.589	0.842	0.676	0.875	0.077	P633
-119.0258	37.6966	-7.015	8.902	-1.281	0.640	0.812	0.117	P634
-119.1380	37.8393	-8.583	9.721	1.230	0.783	0.887	0.112	P635
-119.1467	37.9628	-9.065	8.489	0.545	0.827	0.774	0.050	P636
-119.0837	37.9141	-8.348	9.092	1.202	0.761	0.829	0.110	P637
-118.9435	37.7343	-7.992	7.484	0.497	0.729	0.683	0.045	P638
-118.8687	37.6546	-6.317	8.079	2.001	0.576	0.737	0.183	P639
-118.9604	37.8917	-7.341	9.038	1.606	0.670	0.824	0.146	P640
-118.8519	37.8782	-6.052	8.274	1.619	0.552	0.755	0.148	P641
-118.8167	37.5914	-6.590	7.978	1.564	0.601	0.728	0.143	P642
-118.6982	37.5615	-5.598	7.299	1.423	0.511	0.666	0.130	P643
-118.6844	37.4954	-6.234	6.743	0.818	0.569	0.615	0.075	P644
-118.5935	37.5413	-5.835	6.943	1.885	0.532	0.633	0.172	P645
-118.8200	37.6770	-5.894	7.898	1.003	0.538	0.720	0.091	P646
-118.7677	37.7544	-5.623	7.521	2.535	0.513	0.686	0.231	P647
-119.0192	37.8000	-8.446	9.462	1.145	0.770	0.863	0.104	P648
-118.7362	37.9035	-4.966	7.826	1.392	0.453	0.714	0.127	P649
-118.5549	37.8913	-4.131	6.344	0.688	0.377	0.579	0.063	P650
-118.3870	37.5631	-4.952	5.608	0.053	0.452	0.512	0.005	P651
-118.2385	37.5892	-3.264	4.253	0.641	0.298	0.388	0.058	P652
-118.4717	37.7375	-4.476	5.961	0.406	0.408	0.544	0.037	P653
-119.1502	38.0579	-8.597	8.629	2.208	0.784	0.787	0.201	P654
-118.5611	37.4395	-6.492	7.057	1.054	0.592	0.644	0.096	P724
-119.7456	37.0889	-9.081	9.236	1.244	0.828	0.842	0.113	P725
-118.1467	37.2805	-5.416	4.638	0.304	0.494	0.423	0.028	P726
-118.4668	37.2736	-7.244	7.153	0.829	0.661	0.652	0.076	P727
-119.0569	37.8314	-8.373	9.227	0.673	0.764	0.842	0.061	PMTN
-118.8979	37.6771	-7.455	7.825	1.191	0.680	0.714	0.109	RDOM
-117.0855	36.2179	-3.369	3.710	-0.611	0.307	0.338	0.056	ROGE

Continued on next page

Table S1 – continued from previous page

Lon	**Lat**	V_E **(mm/yr)**	V_N **(mm/yr)**	V_U **(mm/yr)**	σV_E **(mm/yr)**	σV_N **(mm/yr)**	σV_U **(mm/yr)**	**Station ID**
-118.9532	37.6899	-7.905	7.657	-0.379	0.721	0.698	0.035	SAWC
-118.9456	37.6249	-7.790	8.162	0.666	0.711	0.744	0.061	SHRC
-118.8629	37.6189	-6.708	8.118	0.242	0.612	0.740	0.022	TILC
-118.6539	37.6643	-4.630	7.829	0.902	0.422	0.714	0.082	WATC

References

Agnew, D. C. (1997). NLOADF: A program for computing ocean-tide loading. *Journal of Geophysical Research: Solid Earth*, *102*, 5109–5110. doi:https://doi.org/10.1029/96JB03458.

Argus, D. F., Landerer, F. W., Wiese, D. N., Martens, H. R., Fu, Y., Famiglietti, J. S., Thomas, B. F., Farr, T. G., Moore, A. W., & Watkins, M. M. (2017). Sustained water loss in California's mountain ranges during severe drought from 2012 to 2015 inferred from GPS. *Journal of Geophysical Research: Solid Earth*, *122*. doi:10.1002/2017JB014424.

Landerer, F. W., Flechtner, F. M., Save, H., Webb, F. H., Bandikova, T., Bertiger, W. I., Bettadpur, S. V., Byun, S. H., Dahle, C., Dobslaw, H., Fahnestock, E., Harvey, N., Kang, Z., Kruizinga, G. L. H., Loomis, B. D., McCullough, C., Murböck, M., Nagel, P., Paik, M., Pie, N., Poole, S., Strekalov, D., Tamisiea, M. E., Wang, F., Watkins, M. M., Wen, H.-Y., Wiese, D. N., & Yuan, D.-N. (2020). Extending the Global Mass Change Data Record: GRACE Follow-On Instrument and Science Data Performance. *Geophysical Research Letters*, *47*, e2020GL088306.

Luthcke, S. B., Sabaka, T., Loomis, B., Arendt, A., McCarthy, J., & Camp, J. (2013). Antarctica, Greenland and Gulf of Alaska land-ice evolution from an iterated GRACE global mascon solution. *Journal of Glaciology*, *59*, 613–631. doi:10.3189/2013JoG12J147.

Montgomery-Brown, E., Wicks, C., Cervelli, P. F., Langbein, J. O., Svarc, J. L., Shelly, D. R., Hill, D. P., & Lisowski, M. (2015). Renewed inflation of Long Valley Caldera, California (2011 to 2014). *Geophysical Research Letters*, *42*, 5250–5257. doi:10.1002/2015GL064338.

Save, H. (2020). CSR GRACE and GRACE-FO RL06 Mascon Solutions v02, . doi:10.15781/cgq9-nh24.

Save, H., Bettadpur, S., & Tapley, B. D. (2016). High-resolution CSR GRACE RL05 mascons. *Journal of Geophysical Research: Solid Earth*, *121*, 7547–7569. doi:https://doi.org/10.1002/2016JB013007.

Silverii, F., Montgomery-Brown, E. K., Borsa, A. A., & Barbour, A. J. (2020). Hydrologically Induced Deformation in Long Valley Caldera and Adjacent Sierra Nevada. *Journal of Geophysical Research: Solid Earth*, *125*, e2020JB019495. doi:10.1029/2020JB019495.

Wahr, J., Molenaar, M., & Bryan, F. (1998). Time variability of the Earth's gravity field: Hydrological and oceanic effects and their possible detection using GRACE. *Journal of Geophysical Research: Solid Earth*, *103*, 30205–30229. doi:10.1029/98JB02844.